ELSEVIER

RESEARCH: Review

Materials, technological status, and fundamentals of PEM fuel cells – A review

Yun Wang [1,*], Daniela Fernanda Ruiz Diaz [1], Ken S. Chen [2], Zhe Wang [3], Xavier Cordobes Adroher [4]

[1] Renewable Energy Resources Laboratory (RERL) & National Fuel Cell Research Center, Department of Mechanical and Aerospace Engineering, The University of California, Irvine, CA 92697-3975, USA
[2] Sandia National Laboratories, 7011 East Avenue, MS 9154, Livermore, CA 94550, USA
[3] State Key lab of Power Systems, International Joint Laboratory on Low Carbon Clean Energy, Innovation, Department of Energy and Power Engineering, Tsinghua University, Beijing, China, 100084, People's Republic of China
[4] General Motors Japan Ltd., Higashi-Shinagawa Shinagawa-ku, Tokyo 140-8687, Japan

PEM (Polymer Electrolyte Membrane) fuel cells have the potential to reduce our energy use, pollutant emissions, and dependence on fossil fuels. In the past decade, significant advances have been achieved for commercializing the technology. For example, several PEM fuel cell buses are currently rated at the technical readiness stage of full-scale validation in realistic driving environments and have met or closely met the ultimate 25,000-h target set by the U.S. Department of Energy. So far, Toyota has sold more than 4000 Mirai PEM fuel cell vehicles (FCVs). Over 30 hydrogen gas stations are being operated throughout the U.S. and over 60 in Germany. In this review, we cover the material, design, fundamental, and manufacturing aspects of PEM fuel cells with a focus on the portable, automobile, airplane, and space applications that require careful consideration in system design and materials. The technological status and challenges faced by PEM fuel cells toward their commercialization in these applications are described and explained. Fundamental issues that are key to fuel cell design, operational control, and material development, such as water and thermal management, dynamic operation, cold start, channel two-phase flow, and low-humidity operation, are discussed. Fuels and fuel tanks pertinent to PEM fuel cells are briefly evaluated.

The objective of this review is three fold: (1) to present the latest status of PEM fuel cell technology development and applications in the portable and transportation power through an overview of the state of the art and most recent technological advances; (2) to describe materials and water/thermal transport management for fuel cell design and operational control; and (3) to outline major challenges in the technology development and the needs for fundamental research for the near future and prior to fuel cell world-wide deployment.

Introduction

PEM (Polymer Electrolyte Membrane) fuel cell technologies have received world-wide attention in recent years owing to their high efficiencies and low emissions. PEM fuel cells are constructed using polymer electrolyte membranes (notably Nafion®) as the proton conductor and electrochemical catalyst (usually Platinum-based materials) for electrochemical reactions under low temperature. Their noteworthy features include low operating temperature, high power density, and easy scale-up, making

* Corresponding author.
E-mail address: Wang, Y. (yunw@uci.edu)

1369-7021/Published by Elsevier Ltd. https://doi.org/10.1016/j.mattod.2019.06.005

PEM fuel cells a promising candidate as the next generation of power sources for transportation, stationary, and portable applications. Fig. 1 shows a PEM fuel cell structure and major components.

To provide a sense of history, Sir William Robert Grove demonstrated the very first fuel cell in 1839 by showing that the electrochemical dissociation of water was almost reversible using platinized platinum (Pt) electrodes in dilute sulfuric acid [1]. Another milestone was the first practical fuel cell developed by General Electric Company (GE) for the Gemini space mission in 1962. The 1-kW Gemini fuel cell system had a Pt-loading of 35 mg/cm^2 and performance of 37 mA/cm^2 at 0.78 V [2]. Each stack consisted of 31 cells in series with an effective diameter about 22 cm for each cell, bi-porous nickel as electrodes (anode porous Ni and cathode lithiated NiO), and 70–85% potassium hydroxide solution as electrolyte. Water and heat byproducts were removed by circulating hydrogen. The whole stack was enclosed in a thin metallic cylinder, and provided all the electric power for life support and drinking water in the two-week lunar mission. In the 1960s, improvements were made by incorporating Teflon in the catalyst layer directly adjacent to the electrolyte, as was done with the GE fuel cells at the time. Considerable improvements were made from the early 1970s onward with the adoption of the fully fluorinated Nafion® membrane. However, research and development in PEM fuel cells didn't receive much attention and funding from the federal government, in particular the US Department of Energy (DOE), and industry until a few decades ago or so when breakthrough methods for reducing the Pt loading required for PEM fuel cells were developed and subsequently improved by Los Alamos National Laboratory (LANL) and others. Notably, Ian Raistrick [3–5] of LANL came up with a breakthrough technique by applying a solution containing dissolved Nafion® material to the surface of a porous electrode. The electrodes were pressed to the membrane once the solution dried to produce an assembly that contains membrane and electrodes. Wilson [6,7], also of LANL, later invented methods for fabricating repeatable thin-film electrodes bonded to the proton-exchange membrane to generate a membrane electrode assembly (MEA). Combining Raistrick's and Wilson's techniques made it possible to dramatically lower the required precious-metal catalyst loadings by a factor of over 20 while simultaneously improving performance. Another contribution also due to LANL is that by Gottesfeld who proposed to inject a small amount of oxygen-containing air into the fuel stream to oxidatively remove CO from the catalyst surface [8]. This technique enables the direct use of hydrogen-rich gas streams derived from hydrocarbon fuels (such as gasolines, methanol, or natural gases) for PEM fuel cells. Recently, the concept of porous media flow fields was introduced to improve reactant supply and byproduct removal and fuel cell design [9,10]. In 2017, Toyota launched its first commercial fuel cell vehicle, Mirai, at a price less than $59,000 with a total Pt loading of 0.365 mg/cm^2 (anode loading of 0.05 mg/cm^2 and cathode of 0.315 mg/cm^2). The Toyota Mirai fuel cells adopt a carbon-coated Titanium-based porous flow field in the cathode. Though many technical and fundamental breakthroughs have been achieved during the last couple of decades, several challenges such as reducing cost and improving durability remain prior to the world-wide deployment of PEM fuel cells.

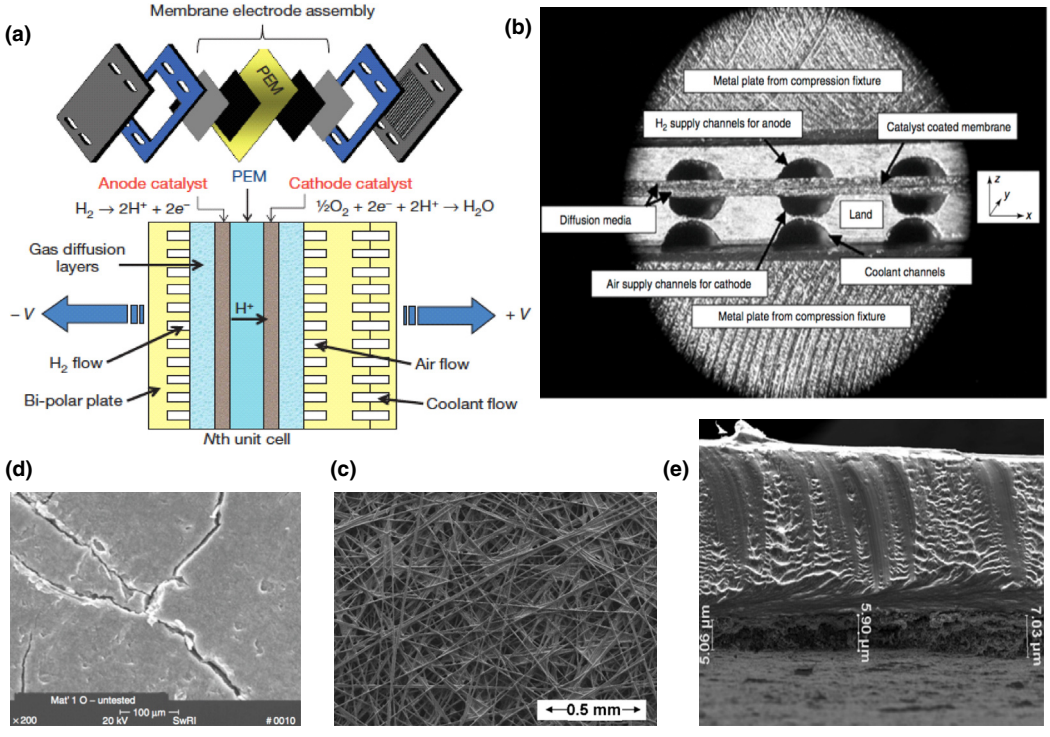

FIGURE 1

(a) PEM fuel cell structure, (b) cross-sectional view; (c) SEM (top view) of a gas diffusion layer; (d) SEM (top view) of a ELAT@ microporous layer; and (e) SEM (cross-sectional view) of catalyst layer and membrane [78,148,296,306].

In the remaining of this section, the current status of PEM fuel cell technology and its portable/transportation applications are first presented, followed by discussions on fuel cell materials, hydrogen tanks, balance of plants (BOP), and fundamentals of fuel cell operation.

PEM fuel cells

The major applications of PEM fuel cells focus on transportation, distributed/stationary and portable power generation. Various fuel cell vehicles (FCV) have been developed and demonstrated, e.g. Honda Clarity, Toyota Mirai, GM ZH2, and Hyundai Tucson FCV, as shown in Fig. 2. In particular, Toyota commercialized their first FCV, Mirai, in 2017. There were nearly 5000 FCVs by the middle of 2018 [11]. Distributed PEM fuel cell power system primarily focuses on small scale power demands (50–250 kW for decentralized use or <10 kW for households) [12]. Early designs considered fuel cells for residential power supply, in which the waste heat of fuel cells can be utilized for household usage – this significantly increases the overall efficiency. Back-up power for banks and telecommunication companies receives growing interests recently because of the extremely high cost associated with power breakdowns. Another promising area is portable electronics or airplane power, considering that the limited energy capacity of batteries unlikely meets the fast-growing energy demand of the modern portable electric devices, such as laptops, cell phones, and military radio/communication devices. PEM fuel cells provide continuous power as long as hydrogen fuel is available, and they can be fabricated in small sizes without efficiency loss. For airplane power, PEM fuel cells show advantages in providing direct electrical power, high power density, and large energy capacity [13]. Both Boeing [14] and Airbus considered PEM fuel cells as auxiliary power for their airplanes. In recent development, PEM fuel cells for long-distance drones have been explored.

As a major milestone in PEM fuel cell commercialization, Toyota introduced their Mirai FCV in 2017. The Toyota Mirai fuel cell system adopts advanced design and materials to achieve a Pt-loading of 0.365 mg/cm^2, 2.0 kW/kg, and 3.1 kW/l for a total of 153 HP generations. A further reduction in fuel cell cost is viable and necessary to compete with internal combustion engines without government incentives. As of June 2018, nearly 5000 FCVs are in operation in the U.S. since 2015. There are more than 20,000 forklifts in the U.S. and more than 20 buses in four states, which are powered by PEM fuel cells. Over 30 hydrogen gas stations are operating and 200 more are planned in the state of California by 2025. Approximately 650-MW fuel cell power were shipped in 2017, about 30% and 100% increase over 2016 and 2015, respectively, among which about 2/3 power was produced by PEM fuel cells in 2016 and 2017 [11].

FIGURE 2

Fuel cell vehicles (FCVs) and fuel cell buses (FCBs). Three FCBs in California were rated around the technical readiness stage of full-scale validation in a relevant environment by NREL: Zero Emission Bay Area Demonstration Group led by Alameda-Contra Costa Transit District (AC Transit), American FCB Project at SunLine Transit Agency, and American FCB Project at University of California, Irvine (UCI) [12,18].

Commercialization and technical barriers

Currently, the two major barriers that still exist are durability and cost [12,15]. For state-of-the-art fuel cells, durability decreases with decreasing platinum group metal (PGM) loading, making it difficult to achieve the DOE durability target while also meeting cost and PGM loading targets (U.S. DOE, 2019). Though Toyota introduced its first commercial Mirai FCV in 2017, the initial sale price before incentives is high in comparison with the vehicles powered by gasoline engines. Significant governmental incentives are needed in order for FCVs to be competitive, cost-wise. The DOE durability test showed that the Toyota Mirai passed the 3000-h real-world driving but failed largely in the AST protocols set by DOE [16,17]. The performance was significantly reduced after 5000 cycles with the CL thickness decreased from ~10 to 3 μm for 1.0–1.5 kV cycle AST. The lifetime target is over 5000 operating hours by 2025 and ultimately 8000 h for automotive, and 25,000 h for buses. As to cost, about 60% cost reduction has been achieved in the past ten years. The current status is $45/kW and $50/kW for 100 and 500 thousand per year product volume, respectively. The 2020 and ultimate DOE targets are $40/kW and $30/kW, respectively, for fuel cells in FCVs, and $600,000 per bus (in comparison with the price ranging from $1.8 to $2.5 M around 2016) for FCBs [18,19]. Among the components, the CLs contribute to the major portion, more than 40% of total fuel cell cost at high volume production (see Fig. 3) primarily due to the use of noble metal catalysts. The target set by the US DOE is 0.125 mg Pt/cm^2 by 2020. As to portable power that ranges from 100 to 250 W, the 2025 DOE targets are $5/W and 5000 h, in comparison with $15/W and 2,000 h at present [15,19].

Role of material and fundamental research

Although the first commercial FCV, Toyota Mirai, was launched in 2017, a few more years is anticipated being required prior to fuel cell fully-worldwide deployment, including the transportation and portable applications. Advancement in materials, control, and fuel cell design is important to reduce system weight, volume, and cost and to improve the durability and performance. In fuel cell operation, multiple interrelated and complex phenomena occur, including mass/heat transfer, electrochemical reactions, and ionic/electronic transport, which govern fuel cell performance. Breakthroughs in material development, acquisition of fundamental knowledge, and development of analytical models and experimental tools are particularly important to the current stage of fuel cell development [12]. For example, non-PMG catalyst and electrode design are critical to fuel cell cost reduction. Advanced control strategies for fuel, water, and thermal management are important for system cost and weight reduction and durability improvement. This review focuses on the discussions of PEM fuel cell applications, technology status, materials, design, balance of plants (BOP), and fundamental research. Although the review attempts to cover the majority of the literature on this topic, there are undoubtedly some that may have been left out.

PEM fuel cell applications and technology status

Transportation and portable power generations are two primary areas for PEM fuel cell applications, which require much attention in fuel cell design due to the space and weight constraints and rapid dynamic power demanding in practice. The power of electric passenger car, utility vehicles, and bus ranges from 20 to 250 kW, and that of small-scale airplanes or drones may vary from 100 W to a few kWs. The portable power usually ranges from 5 to 50 W.

Portable and micro PEM fuel cells

Possibly due to competition from and advancement in battery technologies, the portable fuel cell sector has seen setback in the last several years. As shown in Fig. 4, the number of portable fuel cell shipments has steadily risen from 5000 units in 2008 to more than 21,000 units in 2014. However, the number shipped in 2017 decreased back to the 2008 levels [20–22]. Similarly, as shown in Fig. 4, the total portable fuel cell power or wattage peaked in 2015 but has dropped in the last few years. In this sector, fuel cells provide power for small portable electronics and other portable appliances, non-automotive auxiliary power systems (APUs) and military applications.

In 2012, shipments of portable fuel cell systems and power grew 174% and 25%, respectively, with respect to the previous year. This increase was partly due to the introduction of micro fuel cell chargers for consumer electronics [20]. Nevertheless, in the mid-2010s several key fuel cell companies ceased production and/or transitioned to other power devices [22–26]. In 2015, British Intelligent Energy stopped manufacturing its UPP fuel cell charger and started working on the integration of fuel cells to smartphones and drones [27]. In 2019, Intelligent Energy launched new 2.4-kW fuel cell power product for UAVs [28]. In

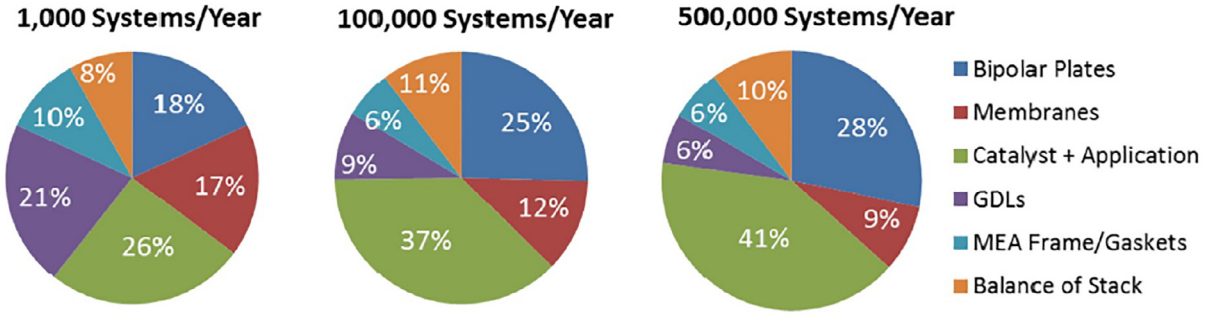

FIGURE 3

Fuel cell cost breakdown [9].

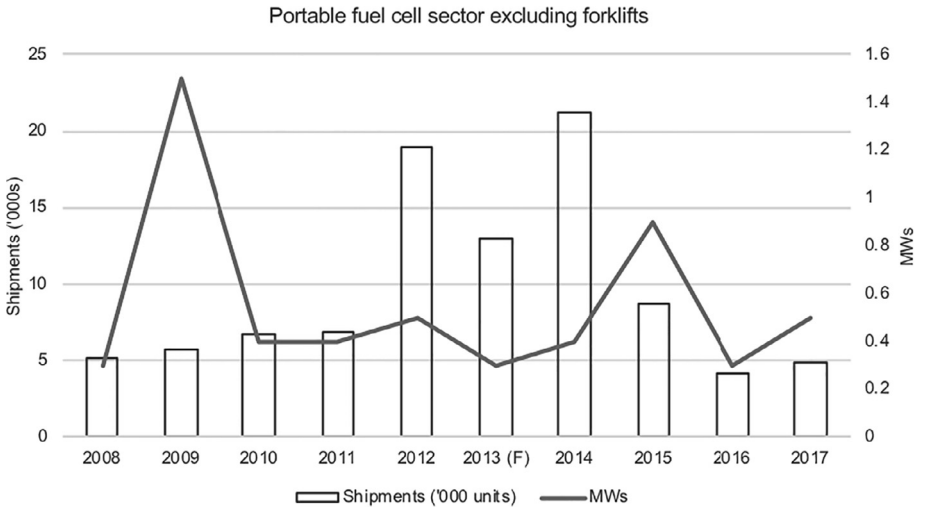

FIGURE 4

Fuel cell shipment and power generation in the portable power sector [12,20–22].

2017, Swedish myFC launched its JAQ Hybrid, a power bank capable of being recharged through an embedded fuel cell. Moreover, the company unveiled a thin fuel cell system, ready to be used in smartphones [29–30] and recently received an order of 4000 JAQ units from the Swedish lifestyle distributor RLVNT and Lightec Japan [31–32]. However, German eZelleron pulled back the release of its portable fuel cell charger Kraftwerk due to an intellectual property dispute [33]. Notwithstanding the insubstantial sales by 2017, consumer electronics remains a high potential market for portable fuel cells. The demand for charging options and long power duration solution is estimated to grow, especially in areas with limited grid access.

For APU (auxiliary power unit) applications, Japanese AquaFairy piloted a water-activated micro fuel cell charger to emergency power units [22,34]. Danish Serenergy provides compact fuel cells using reformed methanol, leveraging on high temperature PEM technology. Its product portfolio features portable air-cooling systems of 350 W and liquid-cooling systems of both 2.5 kW and 5 kW [35–36]. Similarly, Singaporean Horizon Fuel Cell Technologies has been developing mobile PEM fuel cell systems of both 100 W and 200 W, which can be configured together with photovoltaic (PV) and wind power modules [37].

Owing to their low acoustic and thermal signatures, high reliability, quick recharging, and high energy density, portable fuel cells are regarded as a promising power source for military applications [38]. In 2015, Ballard Power Systems (Ballard) acquired Massachusetts' Protonex Technology Corporation, a leading developer of power management and portable fuel cell solutions for militaries [39–41]. Additionally, Ballard agreed to provide their fuel cell expertise to San Francisco-based Ardica Technologies for soldier wearable systems [25,39–40,42]. On this subject, Singaporean HES Energy Systems commercialized wearable fuel cells of up to 30 W continuous power [22,43]. Furthermore, Californian UltraCell is under contract with several US governmental agencies to develop military portable power solutions and has developed mobile methanol reformate systems of up to 165 W [44–46].

Transportation PEM fuel cells

Transportation is a primary area of application for PEM fuel cells because of their zero emission, high energy conversion efficiency, and high-power density. Major motor companies have been extensively developing PEM fuel cell technology to overcome the major barriers to commercialization, including cost, durability, and cold-start capability [12,47–48]. Although many metrics have been met, significant efforts are still needed to reduce cost and improve durability [49–50]. The U.S. currently have over 5000 FCVs and over 30 hydrogen gas stations. In December 2018, the LAX (Los Angeles International Airport) hydrogen station was open for business, which is the 39th retail hydrogen station in California [51]. In March 2019, Germany's H2 Mobility partnership announced the opening of two new hydrogen gas stations, bringing the total number of retail hydrogen stations to 64 in Germany. About 36 more will be available by the end of 2019 [31]. Japan has a roadmap of 800,000 FCVs in the country by 2030 [52]. In addition, fuel cell hybrid electric vehicles (FCHEV) receive much attention, which combine PEM fuel cells with other energy sources, including batteries, flywheels, and supercapacitors. Fig. 5 shows the power and energy properties of several energy sources.

In 2017, Toyota began selling its first commercial FCV Mirai with 3.1 kW/L power density and 114 kW (153 HP) fuel cell stack [53]. The Toyota Mirai reduces the fuel cell stack's weight and volume by removing external humidifiers and adopting a thin membrane (~10 μm), which benefits self-humidification [54]. Honda [55] and Hyundai [56] recently introduced their 366-mile range Clarity and Tucson FCVs, respectively. GM Heritage Center [57] completed the project Driveway initiated in 2007 utilizing 119 Equinox FCVs with total over 3 million miles by 5000 consumers. For extreme field conditions (e.g. military), GM Authority [58] teamed up with the US Army to develop Chevrolet Colorado ZH2 with a 94-kW power fuel cell system. ZH2 is also capable of providing soldiers with 2 gallons of water per hour from its electrochemical reactions. Table 2 compares several major FCV models. Recently, Mercedes-Benz [59] presented pre-

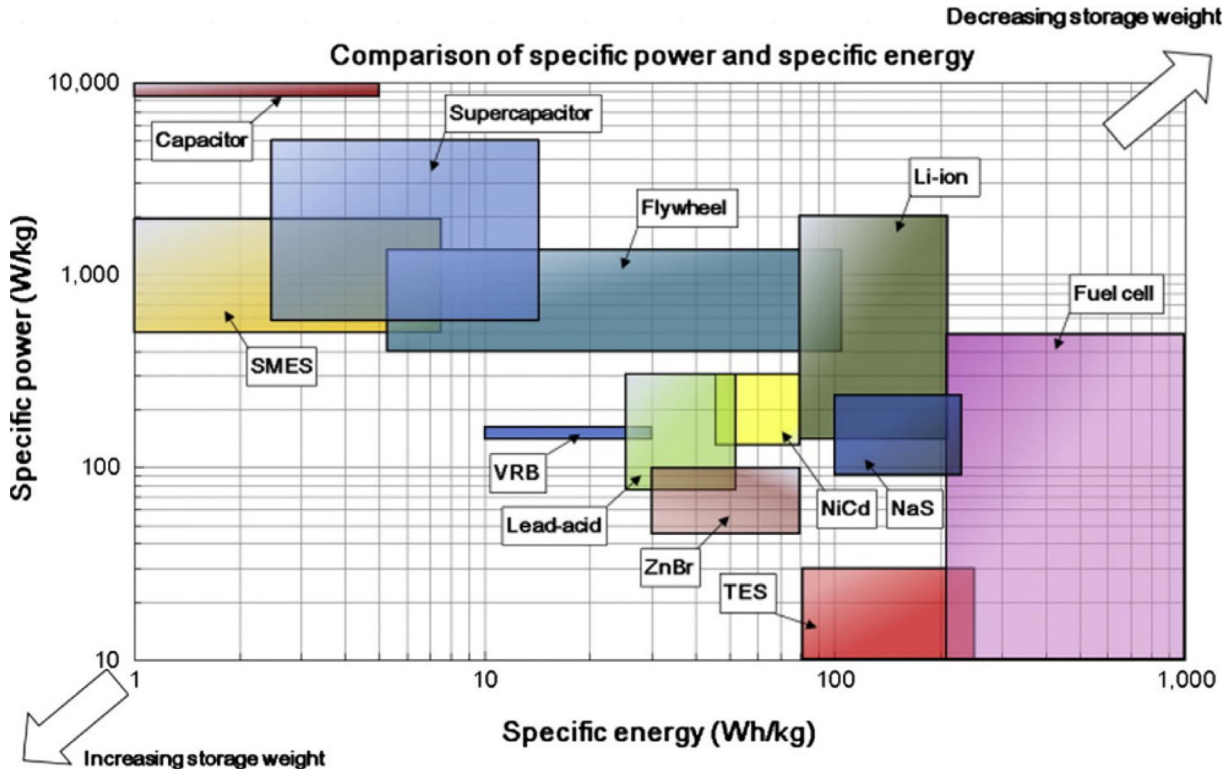

FIGURE 5

Specific Energy vs Specific Power [307].

production models of its new GLC-F-CELL, which combines fuel cell and battery in a plug-in hybrid mode. The GLC-F-CELL carries around 4.4 kg of hydrogen under 700 bar, with a driving range of about 300 miles.

As an extended program of CUTE (Clean Urban Transport for Europe) initiated in 2003, Daimler delivered new Citaro fuel cell buses (FCB) to city of Hamburg with 50% efficiency and 250 km range in 2009. In the U.S., more than 30 FVBs are operated, and they have served about 17 million passengers by 2017 [11]. NREL rates the three FCBs in Table 1 to be around the technical readiness stage of full-scale validation in a relevant environment. In 2015, a FCB surpassed the 2016 durability target, i.e. 18,000 h. In 2016, that FCB reached 23,000 h (almost met the ultimate target of 25,000 h). Another FCB achieved 18,293 h by July 2016. However, capital and operational costs are still much higher in comparison with conventional diesel-based buses. The capital cost in 2010 was around $2.5 million. Around 2016, FCB orders show an average cost of $1.8 million per bus, ~28% decrease. Industry projects a cost of ~$1 million each on an order for 40 buses [18].

In addition to FCVs, airplanes, airships, and marine are potential areas of PEM fuel cell applications [60–61]. A fuel cell system of high energy/power density is ideal for airplane power in two major aspects, including the main power plant for unmanned aerial vehicle (UAV) and auxiliary power units (APU) for large aircrafts. Several studies have been conducted by researchers and major airplane companies to investigate manned fuel cell aircrafts but few practical tests have been reported yet. The critical requirements of UAV are smallscale, longendurance, and long range. AeroVironment succeeded its first test flight using a high-altitude, long-endurance (HALE) aircraft powered by PEM fuel cells with a liquid hydrogen tank in 2003 [39–40]. The flight range was improved up to 9 h by adopting chemical hydride fueling technology developed by Millennium Cell Inc. [62]. The Naval Research Lab (NRL) completed its first 3.3-h flight test using PEM fuel cell and hydrogen gas in 2006 [63]. In 2013, using 5000-psi compressed hydrogen stored in carbon/aluminum pressure vessel, NRL demonstrated a 48-h flight of the Ion-Tiger powered by a 550-W fuel cell stack [64]. The Blue Bird Aero System developed one of the first commercial fuel cell powered UAVs

TABLE 1

Fuel cell configuration and fuel economy for three FCBs [18]·

ID	Period	Fuel Cell OEM	Power (kW)	Energy Storage OEM/capacity	Capacity (kg)/ pressure (bar)	Avg. Speed (mph)	Rang (mile)	Miles per kg or GGE[a]
ACT ZEBA	8/15–7/16	UTC Power	120	EnerDel/17.4 kWh	40/350	8.5	204	5.38
SL AFCB	8/15–7/16	Ballard	150	A123/11 kWh	50/350	13.7	260	5.48
UCI AFCB	1/16–7/16	Ballard	150	A123/11 kWh	50/350	N/A	244	5.15

[a] Gasoline gallon equivalent.

TABLE 2

Fuel cell vehicles [112,211,329–332].

Vehicle Model	Max Power	Fuel Economy MPGe (City/Highway/Comb)	Power Density	Specific Power	Range
Honda FCX Clarity Fuel Cell 2017 (available in market)	103 kW	69/67/68	3.12 kW/L	1.98 kW/kg	366 miles
Toyota FCV Mirai (available in market)	114 kW	67/67/67	3.10 kW/L	2.00 kW/kg	312 miles (122.4 L H_2/70 MPa)
Hyundai Tucson Fuel Cell 2016 (available in market)	100 kW	49/51/50	–	–	265 miles
Roewe 950 Fuel Cell 2014 (concept)	57 kW (motor capacity)	–	–	–	249 miles (−20 °C cold start capability)
Volkswagen Golf Hymotion 2014 (concept)	100 kW	–	–	–	310 miles
Kia Borrego FCEV (concept)	110 kW (motor capacity)	–	–	–	685 km (−20 °C cold start capability)
Daimler GLC F-CELL Hybrid SUV Plug-in	~155 kW	Combined hydrogen consumption: 0.34 kg/100 km	–	–	~430 km (4.4 kg H_2@700 bar) + 51 km (Battery)

in 2009 [65], and UTRC successfully tested a fuel cell rotorcraft for 20-min flight duration [63]. Inha University developed a light-weight UAV with a 200-W stack recording 14-min flight time [66]. H3 Dynamics launched HYWINGS, a fuel cell powered fixed-wing drone, for 500 km and 10 h flight [67]. Protonex, a subsidiary company of Ballard, began selling its fuel cell system for UAV recently [68]. A Canadian-based PEM fuel cell company, EnergyOr Technologies, demonstrated a long-endurance flight with its fuel cell UAV, FAUCON H2 aircraft, which executed a predetermined flight plan for 10 h and 4 min [69]. Table 3 lists fuel cells powered UAVs.

In Spain, Boeing tested a manned two-seat airplane of 16.3-m wingspan for an approximately 20-min flight at 60 mile/h on power solely generated by PEM fuel cells in 2008 [70]. Antares DLR-H2 is one of the first crewed airplanes entirely powered by fuel cells, which demonstrated its capability in 2009 [71]. Based on the ENFICA-FC program, Skyleader Rapid 200 was developed in 2010, capable of a 40-min flight [72]. In 2016, a collaborative group of a small plane maker (Pipistrel), a fuel cell producer (Hydrogenics), University of Ulm and German Aerospace Center tested a flight of HY4, a fuel-cell powered 2-seat airplane with a 9-kg hydrogen tank at the Stuttgart airport in Germany [72].

PEM fuel cells are also being developed as APU in large-scale airplanes [73]. Boeing integrated a fuel cell system in the 787-8 aircraft cargo as 1.5-MW APU, which provides power to the galleys, entertainment units, and backup source for peak electrical loads during descending and landing [74]. Airbus teamed up with DLR to test a fuel cell emergency power system of 20 kW for ATRA research aircraft (A320) [75].

TABLE 3

Fuel cell powered UAV [12,63–67,324].

Organization (year)	Power Source	Reactant Storage Type	Endurance (est.)
Aerovironment, Inc. (2005)	PEM	H_2 Cryogenic	24 h
Naval Research Lab (2006)	PEM	H_2 Gaseous	3.3 h
CSULA/OSU (2007)	PEM	H_2 Gaseous	12 h
KAIST (2007)	PEM	H_2 Sodium Borohydride	10 h
AeroVironment (2007)	PEM	H_2 Sodium Borohydride	9 h
UTRC (2009)	PEM	Compressed H_2	20 min
AFL, Naval Research Lab (2010)	PEM	Metal Hydride	10 h
EnergyOr Technologies (2011)	PEM	H_2	10 h 4 min
Boeing, Lokheed Martin (2011)	SOFC	Propane	8 h
Naval Research Lab (2013)	PEM	Compressed H_2	48 h
H3 Dynamics (2016)	PEM	H_2	10 h

Materials and manufacturing

Fuel cell components

The core component of a PEM fuel cell is the Membrane Electrode Assembly (MEA), which is composed of a polymer electrolyte membrane sandwiched between the anode and cathode electrodes. The electrodes comprise the Catalyst Layer (CL), the Microporous Layer (MPL), and the Gas Diffusion Layer (GDL). The MEA is placed between two Bipolar Plates (BP), where gas flow channels (GFC) are grooved or placed. Fig. 1 displays the major components of a PEM fuel cell.

The hydrogen oxidation reaction (HOR) and oxygen reduction reaction (ORR) take place at the triple-phase boundaries in the anode and cathode CLs, respectively. A PEM fuel cell electrolyte is a polymeric membrane (usually Nafion®), which provides multiple functions, including proton conduction, electronic insulation, and separation of reactant gases [76]. The role of the CL is to facilitate the electrochemical reactions and provide pathways for both reactant transport and electron/proton conduction. A GDL/MPL is placed between the CL and BP to conduct electron and heat, transport gas reactants, and enable water management [77–79].

Table 4 lists the typical thicknesses and materials of the major components in PEM fuel cells. In standard operation, a dry membrane's volume and weight increase by up to 20% and 50%, respectively, due to water uptake [79–81]. Hydration is important to ensure the membrane's proton conductivity, yet too much

TABLE 4

Typical materials of PEM fuel cell components in a stack [12,79,334–337].

	Thickness	Density (g/cm^3)	Typical materials
Polymer electrolyte membrane (PEM)	0.01–0.1 mm	~2	Nafion®
Catalyst layer (CL)	100 nm–0.05 mm	~0.4	Carbon-supported catalyst and ionomer porous composite
Gas diffusion layer (GDL)	0.1–0.4 mm	0.3–0.5*	Carbon fiber-based porous paper
Microporous layer (MPL)	~0.05 mm	0.3–0.5*	Carbon black and PTFE binder
Bipolar plate (BP)	0.3–2 mm	1.7–8**	Carbon-based composites or metals

* Estimate based on graphite carbon density and component porosity.
** Estimate based on graphite and stainless steel densities.

water floods the electrodes and hampers the transport of reactant gases toward the CLs. The optimal membrane water content is determined by several mechanisms in operation, including water generation, the electro-osmotic drag, back diffusion, and hydraulic permeation across the membrane [76,78,81].

Bipolar plates

The practical implementation of fuel cells requires bipolar plates (BPs) to meet stringent performance criteria as outlined in Table 5. Traditionally, BPs are made of graphite with grooved gas flow channels (GFCs). Although having high corrosion resistance and electrical conductivity, graphite possesses large gas permeability and is brittle, making it difficult for mass production and long-term use [82]. Several BP materials have been explored for commercial PEM fuel cells, including carbon composites, aluminum, stainless steel, and titanium.

Carbon composite BPs consist of polymer binder and conductive carbon fillers [83] with the former providing mechanical strength and gas impermeability, and the latter offering the conductive pathways for electron and heat [84]. This type of materials will yield low electrical or thermal conductivity if the constituent carbon fillers are below the percolation threshold [85]. Increasing the filler content or combining multiple types of fillers, such as carbon black, carbon fibers, graphite particles, and carbon nanotubes, will enhance the composite conductivity [86–89], as a result of improved carbon cluster connection. However, excessive fillers will reduce the mechanical strength, causing cracks, or material failure. The geometry or morphology of carbon fillers and the filler content are the key factors determining the composite BP's properties [90]. Fabrication of this type of BPs can follow standard compression molding, thus making it suitable for mass production. In the fabrication process, the homogenous molding material, generally preheated, is first placed in an open, heated mold cavity. The mold is closed with compression to ensure the molding material to completely fill the mold space. Temperature and compression are maintained until the molding material is cured. Non-uniform molding material, heating, or compression can cause local resin rich area or uneven BP thickness, raising the transport resistance or causing concern of gas leakage [91].

Metals have advantages of easy machining, high electric and thermal conductivities, low gas permeability, and robust mechanical strength. Thus, they have been widely investigated as BP material candidates for PEM fuel cells. A major challenge is corrosion in the acidic environment, which results in the formation of oxidants, passive layers, and metal ions. Protective coating is a popular technique to improve metallic BP corrosion resistance [85]. For aluminum BPs, three categories of coating are frequently applied, including metallic, carbon-based, and composite coatings. Pure metallic coating uses noble metals, such as gold, which has a weak bond with the aluminum surface [89] and is also cost prohibitive [90]. Metallic nitrides are another option [91–96]. Both multilayer CrN/ZrN and monolayer CrN were coated by cathodic arc evaporation physical vapor deposition (CAE-PVD), and the coatings met the short-term corrosion resistance requirement [93]. Graphite [94], self-assembled graphene film [95], and diamond-like coatings [96] are typical carbon-based methods, which enable corrosion protection for the substrate. Composite coating combines conductive carbon with polymer matrices, such as the polyaniline-CNT coating and composite of graphite, TiC, and ethylene-tetrafluoroethylene (ETFE), and shows superior corrosion resistance [97–102]. The stainless steel (SS)'s corrosion resistance depends on its specific alloy [99–104]; previous studies [101–106] indicated 316 SS and 316L SS were suitable for BPs. The interfacial contact resistance and corrosion current densities

TABLE 5

Technical targets of BPs for transportation applications [329–339].

Characteristic	Units	2015 Status	2020 Targets
Cost	$/kW	7	3
Plate weight	kg/kW	<0.4	0.4
Plate H2 permeation coefficient	Std cm^3/(s cm^2 Pa) 80 °C, 3 atm 100% RH	0	$<1.3 \times 10^{-14}$
Corrosion, anode	μA/cm^2	No active peak	<1 and no active peak
Corrosion, cathode	μA/cm^2	<0.1	<1
Electrical conductivity	S/cm	>100	>100
Areal specific resistance	ohm cm^2	0.006	<0.01
Flexural strength	MPa	>34 (carbon plate)	>25
Forming elongation	%	20–40	40

of SS BP materials were summarized by Asri et al. [102]. Adding a graphene-Ni layer increases the longevity of the SS BP with a low interfacial contact resistance [103–108]. Active screen plasma nitriding technique was found to improve corrosion resistance and interfacial contact for 316 SS [105]. In addition, the multilayer chromium carbide coating on 316L SS using closed field unbalanced magnetron sputter ion plating (CFUBMSIP) has met the DOE 2020 technical target of both electrical conductivity and corrosion resistance [106]. Titanium nitride (TiN) offers good corrosion resistance, low interfacial contact resistance, good chemical stability, and easy fabrication [107–114], which can be coated by nitrogen plasma immersion ion implantation (PIII) [111], plasma focus [112], pulsed bias arc ion plating (PBAIP), and magnetron sputtering (MS) [109]. Titanium (Ti) substrates are compatible with TiN and thus are an alternative as the BP material [110]. Their performance was summarized by Asri et al. [102] as well. Note that Toyota Mirai adopts Ti for its cathode flow field. In addition, surface defects may occur in coating, leading to pinhole formation and pathways for corrosives to reach the metal substrate [91]. Multi-layered coatings offer an engineering solution to resolve this issue [113–120]. Furthermore, Physical Vapor Deposition (PVD) techniques may cause surface defects, such as craters and droplets [117]. Mitigating these surface defects is an important issue for coating process optimization. Table 6 lists a few coating methods.

Membrane

Desirable membrane materials are those that exhibit high ionic conductivity and simultaneously prevent electron transport and the cross-over of hydrogen and oxygen gases. In addition, they must be chemically stable in the environment with HO and HOO radicals, thermally stable throughout the entire operating temperatures, and mechanically robust. Some early membranes used 183-μm-thick Nafion® 117 to ensure mechanical robustness and separation of the gaseous reactants. With material advance in mechanically reinforced membranes (e.g. Gore-Select™), thin membranes are more popular, such as the 18-μm-thick Gore™ 18. Standard electrolyte membranes operating below 100 °C are based on perfluorosulfonic acid (PFSA). Its hydrophobic perfluorinated backbone provides mechanical support and chemical stability, while the hydrophilic sulfonated side chains promote water absorption forming hydrated clusters [118]. In operation, hydrogen ions (H^+) in form of hydronium ions (H_3O^+) hop and diffuse across the membrane through such hydrated regions via the Grotthus and vehicular mechanisms, respectively [119]. The most commonly used PFSA membrane is Dupont's Nafion®, a copolymer of tetrafluoroethylene (TFE) backbone and sulfonic acid-terminated perfluoro vinyl ether pendant. Nafion® offers high proton conductivity (0.13 S/cm at 75 °C and 100% RH), durability above 60,000 h, and chemical stability. However, it is expensive to fabricate and requires hydration and hence humidification in order to conduct protons [120–126].

Aiming at overcoming these challenges, significant research efforts have been made on modified perfluorinated, partially perfluorinated or non-fluorinated polymers. Dow Company and Solvay launched membranes with shorter side chain (SSC) length, which exhibit higher proton conductivity, crystallinity, and glass transition temperature higher than Nafion® [123]. Gore and Associates introduced a perfluorinated composite membrane reinforced with polytetrafluoroethylene (PTFE), leading to enhanced mechanical and dimensional stability for fuel cells with thin PEMs [124]. Authors of several studies proposed the incorporation of hygroscopic inorganic materials like ZrO_2, TiO_2, $TiSiO_4$, and Silica as fillers in the polymer matrix. These additives result in high water retention, enabling the nanocomposite membranes to maintain their proton conductivity over a broad range of temperatures [125–132]. Yoon et al. [129] proposed mussel-inspired polydopamine-treated composite membranes with self-supported CeOx radical scavengers to mitigate the issues of material loose structure and weak binding among the PEM constituents, therefore improving PEM durability. Sulfonated hydrocarbon polymers constitute a promising alternative due to their low material cost, high water uptake capability at high temperature and low humidity, and good thermal, mechanical, and chemical stability. The most widely investigated systems include polysulfones (PSF), polyetheretherketones (PEEK), and polybenzimidazoles (PBI) [118–123]. PBI is also the promising choice for fabrication of anhydrous high temperature (HT) PEM membranes, which need to be doped with a high boiling point proton solvent, usually phosphoric acid. HT PEM fuel cells operate at about 160 °C, and have gained considerable interest owing to their higher tolerance to CO poisoning and free of liquid water management challenges [130]. Recently, 3M proposed supporting perfluoro imide acid (PFIA) membranes with chemical additives, which meets the 2020 DOE chemical and

TABLE 6

Coating methods and materials for metallic BPs.

Substrate	Coating Material	Method
SS 316	Nitride [105]	Active Screen Plasma Nitriding
Al 5052	TiN, CrN, multilayer C/TiN and C/CrN [92]	Closed Field Unbalanced Magnetron Sputter Ion Plating (CFUBMSIP)
SS 316L	Multilayer coatings (TiN and Carbon); Multilayer Cr–C/a-C:Cr, Zr–C/a-C, Cr–N–C; Cr-C [106,117–119],116	CFUBMSIP
Al 356, 6061	TiN [82]	DC Reactive Magnetron sputtering
SS 304, Ni plated	Graphene [103–108]	Chemical Vapor Deposition (CVD)
Ti	TiN [110]	Multi-arc ion plating
SS316L	TiN ions [107]	Plasma Focus in nitrogen gas
SS304	TiN, Ti_2N multilayer [109]	Pulsed Bias Arc Ion Plating/Magnetron Sputtering
SS316L	CrN, TiN [108]	Cathode Arc Ion Plating

mechanical targets, along with the resistance target for 80 °C [131–136].

Various methods have been proposed to fabricate membranes for PEM fuel cells, including graft polymerization, crosslinking, sol–gel, and direct polymerization of monomers [76]. Graft polymerization can be initiated by utilizing radiation or plasma sources. Plasma-induced polymers present a higher degree of cross-linkage, resulting in thinner membranes with lower electrolyte resistance [133]. Other beams, such as γ-rays and electron, ion, and proton beams, have also been used to initiate grafting through either the simultaneous irradiation or the pre-irradiation method [134]. The crosslinking method seeks to improve the properties of a base polymer by covalently bonding it to a cross-link agent [135]. New cross-linking methods were proposed for more robust and stable membranes [136–141]. The sol–gel technique involves blending a polymer colloidal solution with organometallic precursors via hydrolysis and polycondensation to produce a 3D structure [138–143]. Membranes may be produced through direct polymerization of monomers functionalized by sulfonic acid [140], which has advantages of controllable degree of sulfonation, and avoidable crosslinking and degradation reactions [141].

Anode and cathode

Fuel cell electrode consists of the CL, MPL, and GDL components. To produce a sufficient HOR or ORR rate, the electrochemical reaction interface, i.e. the triple-phase boundary among the ionomer, catalyst particles, and gas phase, is fabricated highly tortuous to maximize the electrochemical catalyst surface area (ECSA). The dominant CL architecture is based on catalyst nanoparticles supported by microscale carbon, impregnated with ionomer thin films [16–17]. The ionomer binder also facilitates proton transport and dissolves oxygen for reaction on the catalyst surface. Excess ionomer will reduce the gas diffusion pathways and obstruct dissolved oxygen access to catalyst. The optimum Nafion® loading is reported to be around 30 wt% [142–147]. In recent, laser induced breakdown spectroscopy (LIBS) was induced to quickly probe the Nafion content, Pt loading [144], and Palladium amount [145] in CLs. Various developers [142] have been exploring novel CL fabrication techniques including ultra-thin CLs, stratified CLs [146–151], ionomer-free CLs, ionomer nanofiber CLs, and nanostructured thin film CLs [142,148]. The CL ink/paste can be applied on either the membrane or GDL/MPL surface by diverse deposition methods, including spraying, painting, screen printing, rolling, decaling, electro-deposition, evaporative deposition, and impregnation reduction [81]. Fig. 6 shows the kinetic activities of main Pt-based catalyst materials and fuel cell performances under various CL material compositions. A recent review on ORR electrocatalyst materials was provided by Shao et al. [149].

The commonly used catalyst and carbon support materials are Pt and carbon black, respectively. Pt has high catalytic activity, but it is scarce, expensive, and sensitive to CO poisoning at standard operating temperature. For this reason, tremendous research activity has focused on reducing the Pt loading and finding an alternative catalyst material [150]. Several of Pt alloys (Pt-Co, Pt-Ni, Pt-Fe, Pt-V, Pt-Mn, and Pt-Cr) exhibit good catalyst kinetics [16–17,155–164].

Pt loading is an important factor in CL development. The DOE target is 0.125 mg/cm^2 for 2020; very recently the 3M Company achieved a total loading of 0.102 mg/cm^2 (including the anode 0.025 mg/cm^2) or 0.172 g/kW under 150 kPa abs with their NSTF [161]. Pintauro [162–167] reported a 0.115 mg/cm^2 loading (anode 0.019 mg/cm^2 and cathode 0.096 mg/cm^2) for their nanofiber-based CLs [162]. However, the NSTF CL is not stable and has not yet been successfully implemented in any commercial units. In addition, Brookhaven National Laboratory (BNL) proposed low-cost Pt monolayer catalysts with noble metal free cores and indicated that nitriding core components improve material stability and reduce Pd content by 50% in comparison with Pt/Pd/C [131,164]. Chong et al. [165] proposed highly active and stable electrocatalysts using cobalt or bimetallic cobalt and zinc zeolitic imidazolate frameworks as precursors. Two catalysts achieved ORR mass activities of 1.08 A/mg$_{Pt}$ and 1.77 A/mg$_{Pt}$ and retained 64% and 15% of initial values after 30,000 voltage cycles.

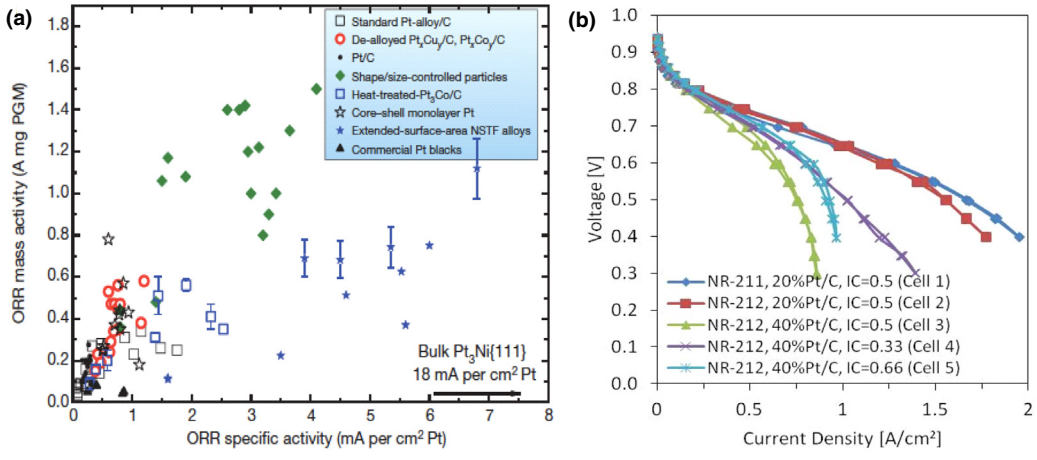

FIGURE 6

(a). Kinetic activities of the main Pt-based electrocatalyst materials [148]; (b). Voltage–current curves for PEM fuel cells at 80 °C and 100 %RH. IC denotes the ionomer to carbon ratio in the CL material [144,296].

In addition, research on new catalyst materials has gained momentum. One method is to replace Pt with another less expensive precious metal, such as ruthenium or palladium [166]. Another approach is to use non-precious metal catalysts (NPMC). Recently, Wu [167] provided a review on NPMC and indicated that M–N–C (M: Fe, Co or Mn) catalysts show encouraging performance. However, stability under acidic conditions remains a challenge to their practical applications. Other reviews were provided by Bezerra et al. on heat-treated Fe- and Co–N/C catalysts [168], Wang on materials such as Cu, Pd/Co, $Mo_{4.2}$-$Ru_{1.8}Se_8$, WC+Ta and $LaMnO_{3+\delta}$ [169] and Zelenay et al. [170]. Very recently, Chung et al. [171] investigated Fe–N–C synthesized with two N precursors that developed hierarchical porosity and demonstrated a current density (at a voltage greater than ~0.75 V) comparable with a 0.1-mg Pt/cm^2 loading cathode. Another study reported new Fe–N–C pyrolyzed materials with a current density of 700 mA/cm^2 at 0.6 V and 120 mA/cm^2 at 0.8 V [172]. Zhang et al. [173] discussed metal–organic frameworks (MOFs), constructed from bridging metal ions and ligands, as a new type of precursors for NPMC synthesis. Two types of metals were investigated, including (i) inactive Zn, Al, or Mg, and (ii) active Fe or Co, which are desirable for preparation of N–C and M–N–C catalysts, respectively.

Another challenge is that CO adsorption at the Pt site causes severe loss in performance – the so called "CO poisoning" phenomena. To improve the CO tolerance of PEM fuel cell, the use of binary Pt–Ru catalysts and oxygen bleeding technique were proposed by Eisman et al. [174] and Gottesfeld [8], and various materials for CO tolerant catalysts (Zeolite support, Pt–Mo, Sulfided catalysts, etc.) are under active research [175]. In addition, Pd also suffers from CO poisoning, which may be addressed by alloying it with less reactive metals while not compromising the catalytic performance [166,176]. Lastly, different carbon-based materials with high porosity and surface area, i.e. single and multi-wall carbon nanotubes, carbon nanofibers, nanohorns, and graphene, have been investigated as catalyst support [177–182].

The optimal CL thickness is determined by the electrochemical kinetics and transport properties. Common Pt-based CLs are 1–10 μm thick to ensure an adequate kinetics for the electrochemical reactions, whereas NPGM-based CLs demand a thickness of 30–100s μm to produce a comparable ORR rate [179–184]. In addition, the reactant species, including protons, electrons, and oxygen/hydrogen gas, need to reach the catalyst sites for the HOR and ORR electrochemical reactions to occur. In the cathode, theoretical analysis indicates that the electron and oxygen transport resistances in a 10-μm thickness CL are usually small [181], but the ionic resistance can be significant, leading to the spatial variation of the ORR reaction rate. A dimensionless parameter $\mathbb{h}\left(=\frac{I\delta_{CL}\gamma_c F}{2R_g T\sigma_m^{eff}}\right)$ quantifies the degree of the reaction spatial variation, i.e. the maximum variation of the dimensionless reaction rate. A thick CL is subject to a large spatial variation, resulting in under-utilization of catalyst and local ohmic loss [146,182].

GDLs and MPLs, together called DM (diffusion media), play multiple roles, including (1) electronic connection between the channel-land structured BP and the CL, (2) passage for reactant transport and heat/water removal, (3) mechanical support to the membrane and CLs and (4) protection of the CL from corrosion or erosion caused by flows or other factors. GDLs are highly porous materials, usually based on carbon fiber papers, e.g. Toray@ and SGL@ GDLs. The GDL dimension is primarily dictated by species/thermal transport, including oxygen, electron, liquid water, and heat. For example, the maximum temperature variation in a GDL can be estimated by Wang and Chen [183]:

$$\begin{aligned}\Delta T_{\max} &= \Delta T_{\max}^{in\text{ - }plane} + \Delta T_{\max}^{thr\text{ - }plane} \\ &= \Delta T_{\max}^{thr\text{ - }plane} f_{\max}\left(\frac{W_{ch}}{H_{GDL}}, \frac{k_{GDL,H}^{eff}}{k_{GDL,W}^{eff}}\right)\end{aligned} \quad (1)$$

where

$$\Delta T_{\max}^{thr\text{ - }plane} = \frac{\frac{1}{2}I(E_o - V_{cell})}{\frac{k_{GDL,H}^{eff}}{H_{GDL}}} \text{ and } f_{\max} = 1 + \frac{W_{ch}^2 k_{GDL,H}^{eff}}{2H_{GDL}^2 k_{GDL,W}^{eff}}$$

A small GDL thickness H_{GDL} leads to a high thermal resistance to the in-plane heat removal under the gas flow channel, which may cause hot-spot formation. In addition, GDLs need to be thick enough to provide mechanical support and erosion protection for CLs. Currently, commercial GDLs range from 100 to 400 μm. The Toyota Mirai's GDL is around 100 μm thick, possibly due to the adoption of a porous media flow field, which provides effective mechanical support and heat/electron pathway via its solid matrix [9].

Nevertheless, such carbon substrates involve a complex manufacturing process and have limited electric and thermal conductivities relative to metals. As alternatives, metallic GDLs were investigated [184–189], which are easy to machine and highly conductive so that the GDL design becomes flexible, e.g. a thin GDL (i.e. small H_{GDL}) and wide GFC (i.e. large W_{ch}). However, they are sensitive to corrosion in the PEM fuel cell operating environment if no effective coating protection is applied. Furthermore, Jayakumar et al. [186] proposed an advanced 3D printing technique to fabricate GDLs, using polyamide as the base powder and adding Ti powder to enhance the electric and thermal conductivities and mechanical properties. Porous silicon GDLs were also proposed using existing silicon fabrication methods (like lithography) for micro/small-scale fuel cells [187].

To improve the multi-phase, particularly liquid, flow characteristics, a MPL is usually integrated between the GDL and CL [188–194]. This layer is composed of carbon black powder with fine pore structure and was reported to benefit water management and fuel cell performance. Due to their finer pore structure than GDLs, MPLs provide better protection for the catalyst nanoparticles and better physical contact with CLs. The MPL thickness is typically around 50 μm. A thick MPL has concerns of raised transport resistances for liquid water removal and oxygen supply.

Balance of Plant

Balance of Plant (BOP) refers to all the peripherals critical to system integration, including air blowers, control strategy, valves, water and thermal management sub-systems, humidifiers, cooling units, insulation, sensors, and power conditioning. Three major components of BOP include the fuel delivery, air delivery, and thermal management sub-systems, as shown in Fig. 7 and

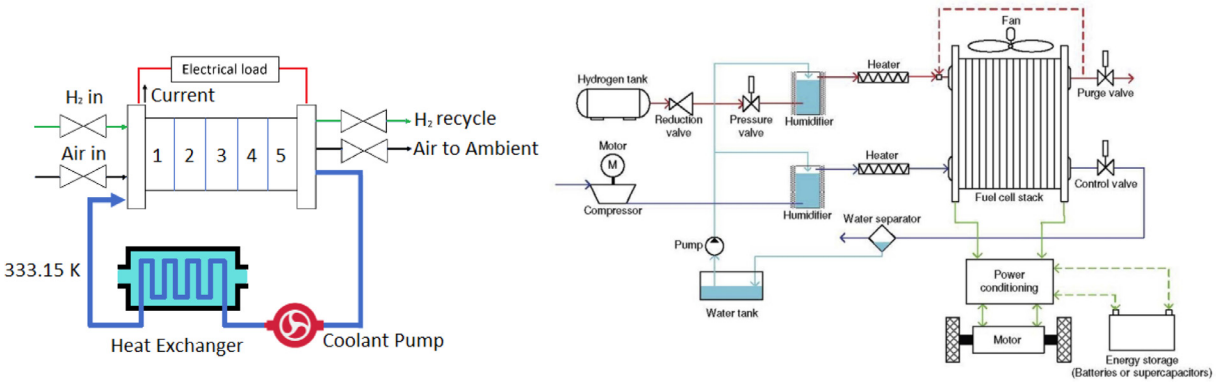

FIGURE 7

BOP designs of a 5-cell stack (left) and a PEM fuel cell stack in FCVs (right) [78,308].

TABLE 7

Components in BOP sub-system [78,331,332].

Air Management	Fuel Management	Thermal Management	Power Units
Compressor	Gas metering	Coolant	AC/DC converter
Humidifier	Humidifier	Pump	Power conditioner
Heat exchanger	Heat exchanger	Heat pipes/Heat spreader	Controller
Sensors	Recirculation pump	Radiator	Wires
Conduits/hoses	Sensors	Heat exchanger	
Flow controller/Valves	Conduits/hoses Flow controller/Valves	Ports and hoses	

Table 7. For direct use of liquid fuels, reformate units need to be equipped to convert the fuels to hydrogen-rich gas. The BOP development is usually regarded as less important than that of the fuel cell reactor, though it contributes to overall system cost, weight, and volume. In addition, the BOP simplification can be achieved by developing more robust fuel cells and MEA components. For example, discovery of new membrane materials having ionic conductivity independent of water will remove the need for external humidification. High-temperature fuel cells demand less thermal management from the BOP.

In the BOP design, the thermal management unit is a major volume/weight contributor. Rejection of waste heat product from PEM fuel cell is much more difficult than that from the internal combustion engines (ICE), providing that fuel cells operate around 80 °C, while the engine surface is about 400 °C. Highly effective heat spreaders, heat pipes, or active liquid/air cooling have been investigated for heat removal from fuel cell stacks. Heat spreaders are advantageous in their simplicity, reliability, and control. Copper is a popular material for spreaders due to its exceptional conductivity (about 400 W/m K). For light weight applications, aluminum is an excellent alternative due to its high conductivity (about 200 W/m K) and low density. Furthermore, CNT (carbon nanotube) and graphene, with their thermal conductivities in the range of 3000–5000 W/m K [191–196], are currently under development as high-rate spreader materials [193–198]. Heat pipes utilize two-phase flow and phase change for thermal transport, thus are highly effective due to the large latent heat release/absorption during the phase change. However, the system requires working fluid and thus has a leakage concern. Active heat pipes need external power input to drive working fluid flows. Liquid cooling adds additional weight and power consumption for the system. Air cooling is advantageous for weight concern, but efficiency suffers. For FCVs, the radiator requires a large surface area in order to reject the waste heat to ambient environment. From Newton's law of cooling, the required surface area is given by $A = \frac{Q}{h\Delta T}$, where Q represents the total heat removal rate, h the heat transfer coefficient, and ΔT the temperature difference between radiator surface and ambient air. Comparing with ICEs where ΔT is about 400 °C, the FCV radiator requires about 5–10 times larger surface area in order to remove the comparable amount of waste heat. Table 8 lists a few potential cooling methods that can be employed by PEM fuel cells.

Humidifiers add water moisture to inlet reactant gases to avoid membrane dry out. Water bubblers are popularly used as humidifiers, which control the liquid temperature and hence the relative humidity (RH) of passing gases. Advanced techniques have been proposed by taking advantage of fuel cell water production or improving their design to avoid water clog or freezing. Honda designed a hollow fiber membrane humidifier, which comprises hollow fiber membranes bundled together in a housing [195]. Hyundai proposed a plurality of hollow fiber membranes having different diameters. The membranes are appropriately arranged to control the flow direction of dry air for uniform humidification [196]. A comprehensive study was conducted by Chen et al. [197] on an external membrane-based humidifier. In general, compact design can be achieved by optimizing water phase change and transport to reduce its add-on volume and weight.

In addition, the oxygen pumping or delivery system can be reduced or eliminated entirely by adopting self-breathing configuration, i.e. ambient oxygen directly diffuses to the cathode. This

TABLE 8

Potential cooling methods and materials for PEM fuel cells [78,248,332–334].

Cooling Method	Techniques/Materials	Advantages/Applications
Heat spreaders	Using highly thermal conductive material (e.g. copper) or heat pipes as heat spreaders	– Simple system – Small parasitic power – Very high thermal conductivity using heat pipes – Common in small-scale or portable PEM fuel cell applications
Air cooling	Separate air flow channels for cooling	– Simple system – Potential integration for fuel cell oxygen supply – Common in small-scale or portable PEM fuel cell applications
Liquid cooling	Cooling channels embedded in BPs using antifreeze coolant	– Large cooling capability – Efficient cooling – Potential integration for fuel cell water management – Common in large-scale or automobile PEM fuel cell applications
Phase change material (PCM) or boiling cooling	Evaporative or boiling cooling utilizing latent heat absorption during phase change	– Simplified system – Elimination of coolant pump – PCM method is suitable to portable fuel cells

configuration, however, is subjected to low power density due to oxygen transport limitation and contamination by impurities in air [78,198], and is only viable to apply for a single- or dual-cell system. For traditional GFC design, the cathode air can be designed and integrated for fuel cell cooling in specific applications.

Hydrogen fuel tanks

Hydrogen gas is considered as the main fuel for PEM fuel cells due to the high efficiency in energy conversion. Direct methanol and ethanol fuel cells are much less efficient due to the large anode electrochemical loss and fuel cross-over. Currently, hydrogen fuel is usually transported and stored in either compressed or cryogenic liquid state. The former is transported in tube trailers typically under 200–500 bar with 250–1000 kg hydrogen payload. The latter is delivered in trailers equipped with vacuum insulated multi-layer dewars capable of over 4000-kg payloads [199]. Hydrogen storage has been an active topic of research for decades. Several storage methods have been proposed for PEM fuel cells, such as compressed tanks, cryogenic method, chemical storage, and hydrides.

Compressed hydrogen is possibly the most common method for FCV hydrogen storage at present. Several factors, including materials, cost, and safety, need to be considered in the tank design due to the high storage pressure and hydrogen reactivity. The current vessels operate under about 70–80 MPa, and thus, the tank materials need to be mechanically robust and withstand hydrogen embrittlement. In addition, lightweight and cost-effective tanks that are easy to operate are important to their world-wide deployment. Carbon fiber-reinforced plastic (CFRP) composites are common vessel materials for compressed hydrogen storage, e.g. type III and IV. The latter is made entirely of CFRP, while the former contains metal-lined CPRP with superior properties but is costly [54,200]. For road driving, additional reinforcement needs to be implemented to provide another layer of protection from collision or fatal accidents. As for fueling stations, hydrogen compressors currently cost about $700,000 for 35 kg/h of capacity (U.S. DOE, 2010). Compressors, storage vessels, and dispensers are usually made of a variety of steels and they experience fatigue loading under a hydrogen pressure as high as ~900 bar. Nozzles may expose to freezing temperature as low as −40 °C, that can exacerbate hydrogen effects in certain steel alloys. Currently, a nozzle cost approximately $7000, and a dispenser breakaway valve is commonly about $3000 in price [201].

The cryogenic method significantly increases the volumetric energy density of hydrogen by liquefaction. For example, the density of liquid hydrogen (LH_2) is 71 kg/m^3 at 1 bar and 20 K, which is much higher than that (40 kg/m^3) of H_2 compressed at 700 bar and 288 K [199]. Currently, commercial technologies have been developed for liquefaction, insulation, transportation, and transpiration cooling. In general, LH_2 storage is only for a short-term hydrogen use because of boil-off loss resulting from heat transfer. If the boil-off is not controlled, the entire container of stored LH_2 will evaporate in about two weeks. In addition, liquefying hydrogen consumes at least 35% of the fuel's energy, about three times more than H_2 compression to 690 atm. In addition, the energy density of LH_2 is ca. 8 MJ/L, substantially less than that of gasoline (32 MJ/L) and diesel fuel (36 MJ/L) [200,202].

Metal hydride storage has received a lot of attention due to their potential for very high capacities on both a gravimetric and volumetric basis. For example, Alane (aluminum hydride, AlH_3) contains 10.1 wt% of hydrogen with a density of 1.48 H_2 g/mL. Lithium borohydride ($LiBH_4$) and sodium borohydride ($NaBH_4$) have a hydrogen content up to 18 wt%. Table 9 lists the hydrogen contents in several materials. A main barrier to the practical use of metal hydrides is the prohibitively high temperatures and pressures necessary for reversible operation [199]. In order to qualify as a H_2 storage material for FCVs the reaction kinetics must favor low energy H_2 desorption or sorption to avoid overall efficiency loss. Alane is in general metastable at room temperature, and thus, its decomposition is very slow and demands a large amount of energy input for hydrogen release. $LiBH_4$ and $NaBH_4$ decompose under a temperature >673 K. Thus, their use is greatly limited and destabilization techniques have been extensively investigated [203].

Fundamentals for fuel cell materials and design

Elucidating the fundamentals of PEM fuel cells is vitally important to technology advancement, barrier breakthroughs, and

TABLE 9

Hydrogen contents in storage method/materials [78,200,336].

Storage method/material	Number of H atoms per cm^3 ($\times 10^{22}$)	Wt% hydrogen
H_2 gas (197 atm)	0.99	100
H_2 liquid (20 K)	4.2	100
H_2 solid (4 K)	5.3	100
MgH_2	6.5	7.6
Mg_2NiH_4	5.9	3.6
$FeTiH_{1.95}$	6.0	1.89
$LaNi_5H_{6.7}$	5.5	1.37
$ZrMn_2H_{3.6}$	6.0	1.75
VH_2	11.4	2.10
H_2O (Liquid, 25 °C)	6.67	11.1
CH_4 (Liquid, −162 °C)	6.35	24.9
AlH_3	8.90	10.0
$LiBH_4$	7.36	18.4
$NaBH_4$	6.81	10.6

optimal design. Outlined below are several key aspects of fundamentals for fuel cell materials and design. Table 10 lists the material and electrochemical properties of PEM fuel cell, and Table 11 provides the first-principle-based, fundamental equations that govern fuel cell operation.

Humidification-free operation

The ionic conductivity of electrolyte membrane is critical to the ohmic voltage loss. Perfluorosulfonic acid (PFSA) polymer membrane, such as Nafion® from DuPont, and ionomers from 3 M and Solvay, has been widely and dominantly used in PEM fuel cells. The ionic conductivity of this type of membrane is a function of water content; a dry membrane reduces ionic conductivity and thus increases the ohmic voltage loss. In practice, external humidifiers are usually equipped to improve membrane hydration by humidifying inlet reactant gases [204–209]. Two major approaches have been attempted to reduce the need for humidifiers: one is to search for new membrane materials with ionic conductivity less dependent on water; the other is to promote internal water humidification.

For the first approach, attempts have been made to develop proton-conducting membranes suitable for high-temperature and low-humidity operation [206–211]. It showed that blending with sulfonated polymer and non-volatile and thermally stable ionic liquid leads to an ionic conductivity over 0.01 S/cm. However, blending may decrease backbone crystallinity, causing mechanical failure [207–219]. Incorporating nanoparticles as additives or fillers has also been investigated. Graphene oxide (GO) contains both hydrophilic and hydrophobic functional groups. In GO nanocomposite membranes, the hydrophilic groups hold water, which improves proton conductivity. They also showed mechanical and chemical stability and low permeability [216–227]. Carbon nanotube (CNT) is another promising filler with its transport properties altered by the internal filling materials [224–229]. It has been reported that water spontaneously fills the hydrophilic interior of a CNT, enabling water movement and proton transport [226]. Molecular dynamics (MD) simulation indicated that the hydrogen bonding between water molecules creates strongly connected one-dimensional

TABLE 10

Material and electrochemical properties of PEM fuel cells [12,336–339].

Description	Unit	Value
Electrochemical kinetics		
Exchange current density (Anode, Cathode)	A/m^3	10^9, 10^3–10^4
Faraday constant	C/mol	96,487
Electrical conductivity of GDLs, BPs	S/m	300, 20,000
Species transport properties		
H_2/H_2O diffusivity (H_2-H_2O) at standard condition	m^2/s	$8.67/8.67 \times 10^{-5}$
O_2/H_2O (v) diffusivity in the air at standard condition	m^2/s	$1.53/1.79 \times 10^{-5}$
Viscosity at 80 °C (H_2/Air)	m^2/s	9.88×10^{-6}/ 1.36×10^{-5}
Thermal properties		
H_2 /N_2/O_2/H_2O(v) thermal conductivity	W/m K	0.170/0.024/ 0.024/0.024
Anode/cathode GDL through/in-plane conductivity	W/m K	0.3–3/21
Anode/cathode CL conductivity	W/m K	0.3–1.5
Membrane thermal conductivity	W/m K	0.95
MPL thermal conductivity	W/m K	0.05–0.12
Anode/cathode bipolar plate thermal conductivity	W/m K	>10.0
H_2 /N_2/O_2/H_2O(v)specific heat at 80 °C	J/kg K	14,400/1041/917/ 2000
Anode/cathode GDL heat capacity	J/K m^3	5.68×10^5
Anode/cathode CL heat capacity	J/K m^3	1.69×10^6
Membrane heat capacity	J/K m^3	1.65×10^6
Anode/cathode bipolar plate heat capacity	J/K m^3	1.57×10^6
Latent heat of sublimation	J/mol	5.1×10^{-4}
Material properties		
Permeability of anode/cathode GDL	m^2	10^{-12}
Permeability of anode/cathode CL	m^2	10^{-14}–10^{-13}
Anode/cathode GDL porosity		0.4–0.88
Anode/cathode CL porosity		0.3–0.5
Ionomer volume fraction in CL		0.13–0.4
Equivalent weight of ionomers	kg/mol	0.9, 1.1 or 1.2*
GDL surface roughness	μm	8
Dry density of membrane	kg/m^3	1.98×10^3*

* Several typical Nafion® membranes.

water nanowires, enabling proton migration inside single-walled CNT [227]. Consequently, adding CNTs to the nanochannels in Nafion® helps improve proton conductivity [228–240]. TiO_2 is also investigated as a hydrophilic filler for Nafion®, which enables better mechanical, thermal, and water uptake properties [237–245]. Its morphological features also greatly affect its role in the membrane performance [126,242]. Perovskite-type oxides and zeolites are potential nanocomposite due to their chemical stability and low cost. The perovskite structure $BaZrO_3$ nanoparticles provide a special pathway for hydrogen transport, therefore improving the proton conductivity of PBI (polybenzimidazole) membranes [243]. In addition, Zeolite is hydrophilic with water sorption capacity being enabled by its charged anionic framework, high pore volume, and large surface area, thus improving Nafion's proton conductivity [244–249]. For high temperature membrane materials, readers are referred to recent reviews [246–251]. Table 12 shows membrane materials for high-temperature and low-humidity operation.

TABLE 11

Governing equations for PEM fuel cell design, control, and material selection [10,78,339].

Continuity equation: $\varepsilon\frac{\partial \rho}{\partial t}+\nabla\cdot\left(\rho\vec{u}\right)=S_m$

Momentum conservation: $\frac{1}{\varepsilon}\left[\frac{\partial \rho\vec{u}}{\partial t}+\frac{1}{\varepsilon}\nabla\cdot\left(\rho\vec{u}\ \vec{u}\right)\right]=-\nabla P+\nabla\cdot\tau+S_u$

Energy conservation: $\frac{\partial \bar{\rho}\bar{c}_pT}{\partial t}+\nabla\cdot\left(\gamma_T\rho c_p\vec{u}\ T\right)=\nabla\cdot\left(k^{eff}\nabla T\right)+S_T$

Species conservation (H_2O/H_2 /O_2/N_2):

$$\varepsilon^{eff}\frac{\partial C^k}{\partial t}+\nabla\cdot\left(\gamma_c\vec{u}C^k\right)=\nabla\cdot\left(D^{k,eff}\nabla C^k\right)-\nabla\cdot\left[\left(\frac{mf_l^k}{M^k}-\frac{C_g^k}{\rho_g}\right)\vec{j}_l\right]+S_k$$

Charge conservation (electrons): $0=\nabla\cdot\left(\sigma^{eff}\nabla\Phi_s\right)-S_\varphi$

Charge conservation (protons): $0=\nabla\cdot\left(\kappa^{eff}\nabla\Phi_e\right)+S_\varphi$

Where

	S_m	S_u	S_k	S_φ	S_T
GFC	0	0 or $-\frac{\mu}{K_{GFC}}\vec{u}$	0	–	S_{fg}
DM	0	$-\frac{\mu}{K_{GDL}}\vec{u}$	0	0	$\frac{i^{(s)2}}{\sigma_s^{eff}}+S_{fg}$
Catalyst Layer	$M^w\nabla\cdot\left(D_m^w\nabla C^w\right)+\sum_k S_kM^k$	$-\frac{\mu}{K_{CL}}\vec{u}$	$-\nabla\cdot\left(\frac{n_d}{F}i_e\right)$ $-\frac{s_kj}{n_kF}$	j	$j\left(\eta+T\frac{dU_o}{dT}\right)+\frac{i^{(m)2}}{\sigma_m^{eff}}+\frac{i^{(s)2}}{\sigma_s^{eff}}+S_{fg}$
Membrane	0	–	0	0	$\frac{i^{(m)2}}{\sigma_m^{eff}}$

Electrochemical Reaction:
$\sum_k s_kM_k^z=ne^-$
In PEM fuel cells, there are:(Anode)
H_2–$2H^+=2e^-$(Cathode) $2H_2O$–O_2–$4H^+=4e^-$

Where

$M_k\equiv$ chemical formula of species k
$s_k\equiv$ stoichiometry coefficient
n $\equiv$ number of electrons transferred

Note: n_d is the electro-osmotic drag coefficient for water. For H_2 and O_2, $n_d=0$.

TABLE 12

Membrane materials for high-temperature or low-humidity operation.

Base	nanocomposite additive	Method & performance
SPEEK/PVA	SGO/Fe_3O_4	Solution casting; 0.084 S/cm @ 25 °C [220]
SPEEK	SGO	0.055 S/cm @ 80 °C and 30% RH [218]
SPEEK	Polydopamine-modified GO	0.498 S/cm [217]
Nafion®	GO with 3-mercaptopropyltrimethoxysilane (MPTMS)	4 time higher than Nafion® @ 120 °C and 25% RH [216]
Nafion®	GO	Spin-coating [221] Layer-by-layer self-assembly [219,223]
Nafion®	Polyoxometalate modified GO	10.4 mS cm^{-1} @ 20% RH and 80 °C [222]
Nafion®	SiO_2-PTA	[228]
Nafion®	PWA-filled CNTs	0.202 S cm^{-1} @ 90 °C [236]
SPAEK–COOH	Polycation chitosan (CTS) and Negatively charged inorganic particle PTA	Layer-by-layer self-assembly [229]
SPEEK	Silica-coated CNTs	10^{-2} S cm^{-1} @ room temperature [235]
SPEEK	Sulfonated halloysite nanotubes (SHNTs)	Facile distillation precipitation polymerization; 0.0245 S cm^{-1} [234]
Nafion®	Im-CNT-0.5 wt.%	[233]
	Sulfonated multi-walled CNT sulfonated PES (s-MWCNT-s-PES) Sulfonated PVA/sulfonated multi-walled CNT (s-MWNTs/s-PVA)	[231–236]
Nafion®	Propylsulfonic functionalized titania (TiO_2-RSO_3H)	0.08 S cm^{-1} @ 140 °C [240]
SPEEK	Phosphonic acid-functionalized titania nanohybrid	Enhanced proton conduction by 25%[241]
	Sulfated nanotitania (TS), sulfonated polysulfone (SPSU), nitrilotri(methyltriphosphonic acid) (NMPA)	Ternary mixtures; 0.002 S/cm @ 150 °C [239]
Nafion®	TiO_2	Sol–gel Casting; Increased performance @ 110 °C [237]
Nafion®	Amine-tailored titanate nanotubes	4–5 times higher proton conductivity [238]
PBI	$BaZrO_3$ $SrCeO_3$	Increased water uptake and proton conductivity [243]
Nafion®	Zeolite	Solvent casting; increased water uptake and proton conductivity [245]
SPEEK	Ferrierite zeolite	Improved mechanical strength and water retention [244]

For low-humidity operation, the counter-flow configuration has been proposed to improve internal humidification, as shown in Fig. 8(a). For the co-flow configuration in which the anode and cathode gas streams are arranged in the same direction, dry inlet reactant gases will dry out the inlet area of the membrane, while the outlet region will likely be subjected to flooding due to water production from fuel cells. This leads to a dilemma in the fuel cell design to balance the mitigations of inlet dryness and outlet

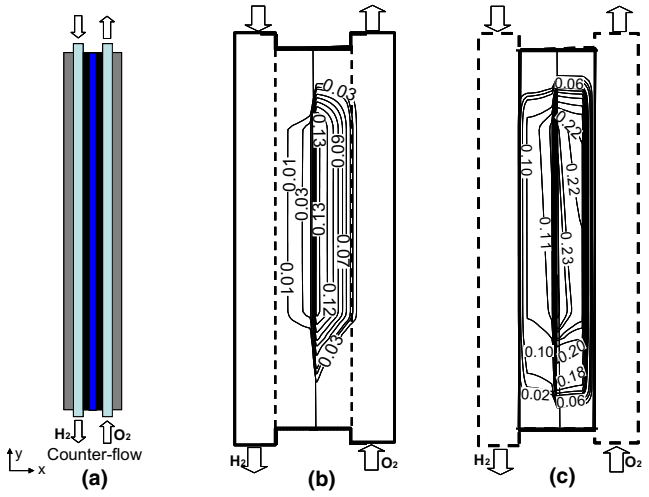

FIGURE 8

(a) Counter-flow configuration, and liquid water saturation contours; (b) under the channel and (c) under the land [309].

flooding. The counter-flow configuration effectively resolves the issue by circulating water inside the fuel cell, realized by the water transport via the membrane from the wet outlet to the dry inlet. This water circulation leads to a much larger area of hydrated MEA even under low-humidity inlet condition, as shown in Fig. 8(b) and (c). Another way is to increase water retention in the MEA. Adding MPLs over the MEA introduces a barrier to both vapor and liquid water transport. The transport resistance is determined by both their pore structure and wettability, which can be modified in the fabrication process, e.g. adjusting the PTFE loading. In addition, the membrane water content can be self-regulated by coating a hydrophobic film with nanoscale cracks ('nanocracks'), which function as valves to retard water desorption and to maintain the membrane proton conductivity on dehumidification, as shown in Fig. 9.

Using thin membranes reduces both proton and water transport resistances, therefore improving internal humidification through the water exchange between the anode and cathode sides and mitigating the anode dryness caused by water electro-osmosis. The transport resistance is proportional to the membrane thickness. For proton transport, a membrane of 2 times thinner, e.g. from Nafion® 112 (~51 μm) to Gore 18 (~18 μm), will yield approximately 70% reduction in the ohmic voltage loss under identical conditions. As to water transport, back diffusion permits the cathode water diffuses to the anode via the membrane. A thin membrane will reduce the back-diffusion resistance, by shortening the transport distance, therefore improving anode rehydration. However, thin members are susceptible to mechanical damage or material degradation (e.g. pin-hole formation or cracks), thus mechanical support either added into Nafion® membrane (e.g. Gore series) or external support from GDLs is important. Toyota Mirai uses ~10-μm reinforced members and a porous media flow field over the cathode GDL to improve mechanical support. In addition, thin membranes may suffer worse hydrogen crossover, which reduces fuel cell performance and durability.

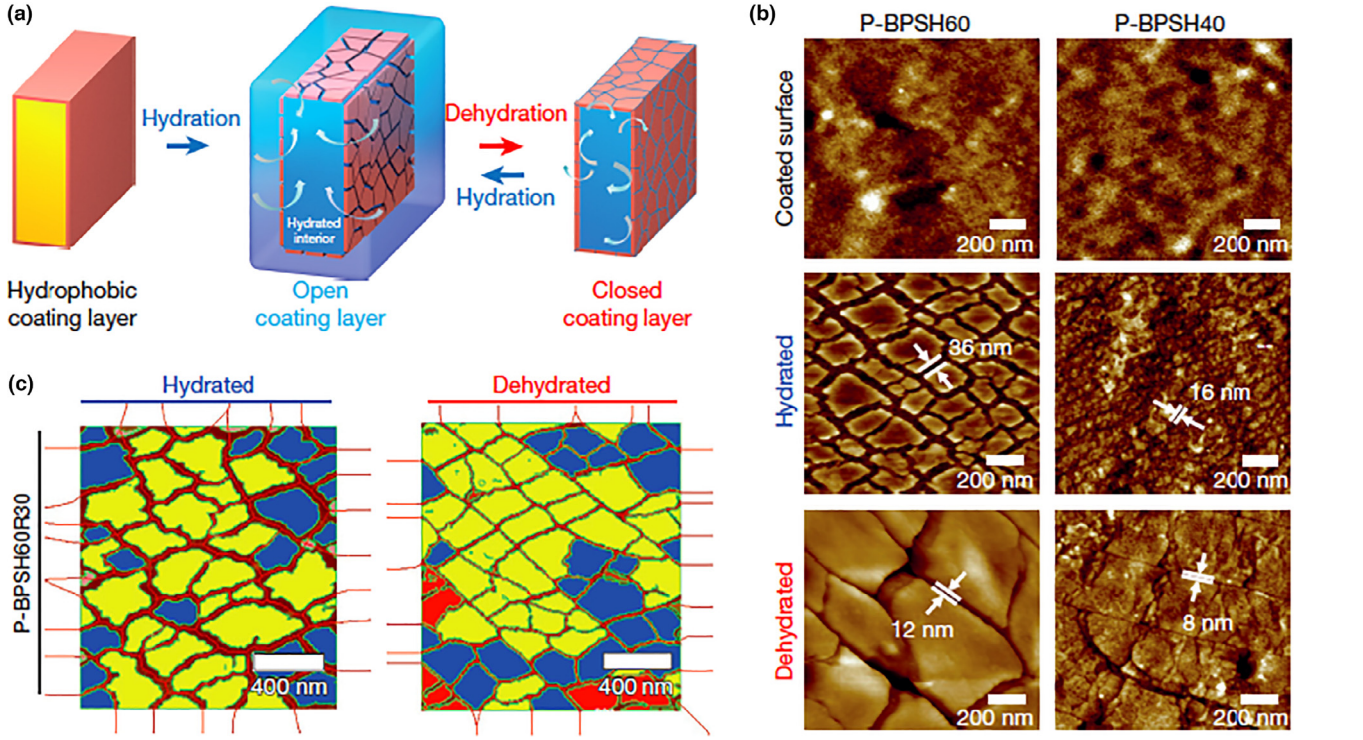

FIGURE 9

Self-humidifying nanovalved membrane: (a). A hydrophobic coating layer provides a self-controlled mechanism for water conservation using nanocracks. (b). AFM images of the self-controlled mechanism of plasma-coated membranes. (c). Voronoi diagram analysis and tessellation entropy verified controllable nanocrack surface pattern images of plasma-coated membrane [310].

Liquid water removal in electrodes

Excessive liquid water hinders the reactant delivery to the catalyst sites, thus increasing the concentration polarization. This is generally referred to as "flooding" phenomena, which raise multiple concerns, including material degradation, performance reduction, and local reactant starvation. In this regard, liquid water transport and its impact on the porous electrodes, including GDL, MPL, and CL, are important to material development and component design for fuel cells.

CLs are the component where the HOR and ORR electrochemical reactions occur, and they contain ionomer and PTFE binder that make CLs hydrophobic to avoid "flooding". Water is essential to the function of the ionomer phase in CLs to conduct protons for the reactions. CL dryness may occur in the anode, which loses considerable water to the cathode by water electro-osmosis. The anode CL ohmic loss can be larger than that of the membrane because of the small content and tortuous structure of the ionomer phase and has been reported to dominate the fuel cell voltage under certain conditions [248]. In this regard, thin anode CLs are beneficial to reducing the ionic resistance and associated ohmic voltage loss. Toyota Mirai FCVs have a ~2.3-μm-thick anode CL, in comparison with a ~10-μm cathode CL. Liquid water normally transports via both pore space and ionomer network. The liquid saturation was estimated to be small ~1% in its spatial through-plane variation across a ~10-μm-thick CL under 1 A/cm^2 [182]. Two major mechanisms have been proposed to account for liquid water's impact on catalyst activity, including the surface area reduction and oxygen transport resistance [78].

Liquid water flow in the porous GDLs is mainly driven by the capillary pressure, generally given by the Young–Laplace $\left(\Delta P = \sigma\left(\frac{1}{R_1}+\frac{1}{R_2}\right)\right)$. In porous media, the Leverett function is frequently adopted to express the capillary pressure as a function of saturation, which may not be directly applicable to fuel cell components because it was formulated originally for water transport in soils. Fig. 10 compares the Leverett function with a few sets of data. In addition, GDLs are usually rendered hydrophobic to facilitate liquid water drainage. Polytetrafluoroethylene (PTFE, a.k.a. DuPont's Teflon™) is commonly added to render the GDL hydrophobicity. To probe the liquid water content in fuel cells, high-resolution neutron, and X-ray radiographies have been employed [249–257]. For example, the Sandia National Laboratories Team in collaboration with researchers at National Institute of Standard and Technology [254–262] employed neutron radiography to probe in real time the liquid water in an operating PEM fuel cell under varying current density and temperature and in-situ high-resolution radiography to quantify the cross-sectional liquid water profile. Lehmann et al. [259] outlined the application of neutron radiography to fuel cells and other research areas. In general, a level of water saturation in average around 10% was reported, and local GDL structural properties may greatly impact local liquid distribution.

Another important mechanism for liquid water transport is through water vapor diffusion and phase change, driven by the temperature gradient. It is conventionally referred to as heat pipe effect, which transfers heat through working fluid flows and phase change. Its effective conductance is given by:

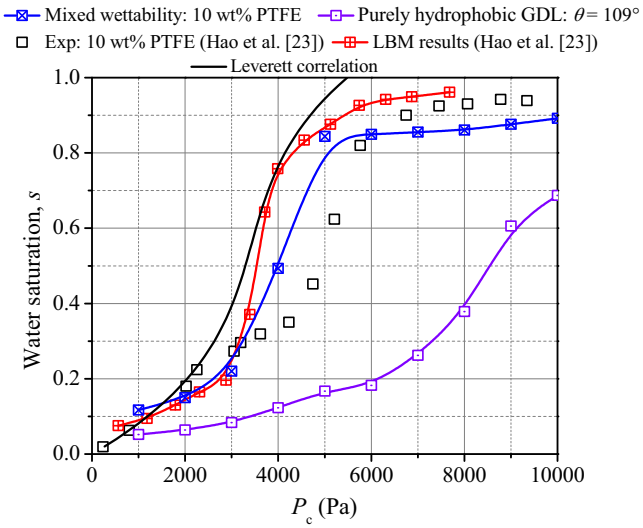

FIGURE 10

Comparison of P_c-s curves obtained from VOF simulations [269], LBM simulation and X-ray experimental data [311] for GDLs with 10 wt% PTFE loadings. Parameters for the Leverett J function model: permeability $K = 4.24 \times 10^{-12}$ m^2, porosity $\varepsilon = 0.74$ (10 wt% PTFE) and 0.66 (20 wt% PTFE), contact angle $\theta = 109°$ [312].

$$k_{fg}(T,P) = h_{fg} M_w D_g^{w,eff}(T,P) \frac{dC_{sat}(T)}{dT} \quad (2)$$

where h_{fg} is the latent heat, M_w is the water molecular weight, $D_g^{w,eff}$ the effective diffusivity, and C_{sat} the saturation water vapor concentration. $k_{fg}(T,P)$ is about ~0.42 W/m K at 80 °C and 0.56 W/m K at 90 °C [260]. Because the temperature gradient that drives vapor diffusion is toward the land, the heat pipe effect raises liquid level under the land. In addition, the heat pipe effect provides a novel way for water management by mitigating liquid water's impact via evaporation. A dimensionless parameter Da (the Damköhler number) was introduced by Wang and Chen [183] to compare the water vapor removal rate with the production rate:

$$\mathrm{Da} = \frac{\text{Rate of water production}}{\text{Rate of water removal via vapor diffusion}} = \frac{\mathrm{IH_{GDL}}}{2\mathrm{FD_g^{w,eff}}\Delta\mathrm{C^w}} \quad (3)$$

where H_{GDL} is the GDL thickness, F the Faraday constant, I current density, and ΔC^w the difference between the saturated water concentration at the GDL–CL interface and vapor concentration in the channel gas steam. Wang and Chen [261] indicated that Da of less than 1 will vaporize the liquid water under the GFC centerline by waste heat, leading to a highly-humidified GDL region free of liquid water. The value of Da is determined by operating temperature, thermal in-plane conductivity, and GFC width.

MPLs play an important role in the water management of electrodes. Gostick et al. [262] indicated that the saturation in GDLs for water breakthrough is drastically reduced from ca. 25% to ca. 5% in the presence of MPL. Lee et al. [263] employed synchrotron X-ray radiography with an effective spatial resolution of 10 μm to investigate liquid water distribution in a fuel cell with MPLs ranging from 0 to 150 μm, indicating the MPLs significantly reduced the water content at the CL–GDL interface and a thicker MPL reduces liquid water accumulation at the GDL–MPL interface. Zhang et al. [234] reconstructed the MPL structure using FIB/SEM tomography at a resolution of 14 nm and investigated its impacts on water and oxygen transports, see Fig. 11. They reported that water is unable to move through a highly

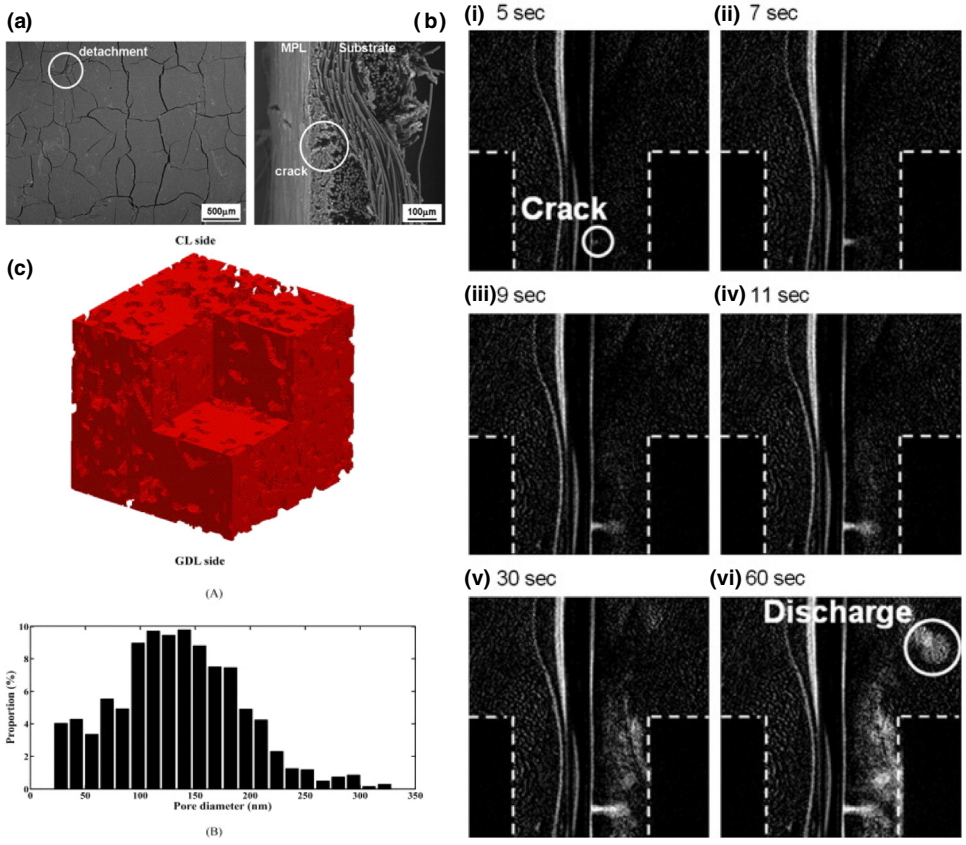

FIGURE 11

(a) MPL surface and the cross-sectional image; (b) Liquid water accumulation and discharge behavior in operating fuel cell [252]; (c) MPL 3D image and the pore size distribution estimated from the FIB/SEM tomography [234].

hydrophobic MPL, and the interaction of the bulk and Knudsen's diffusions creates an extra resistance, thus the conventional model overestimates the effective diffusion coefficient. It was also shown that liquid water may accumulate at the MPL–GDL interface as revealed by the X-ray [264] or modeling methods [265]. Using neutron radiography, Oberholzer et al. [266] indicated that absence of the cathode MPL shifts water accumulation peak toward the electrode and leads to electrode flooding and/or water film formation. Cho et al. [267] showed that large MPL penetration into GDLs improved water management and hence fuel cell performance, and low MPL–GDL binding may cause loss of MPL materials. Öztürk et al. [268] proposed two different molecular weights (MW) of polydimethylsiloxane (PDMS) polymer as alternative hydrophobic materials to conventional PTFE and fluorinated ethylene propylene (FEP) in MPLs. Low MW PDMS polymers showed better fuel cell performance than PTFE and FEP. Sasabe et al. [252] indicated that there exist cracks in MPLs, which greatly influence liquid water transport, see Fig. 11.

Though fundamental models have been developed to elucidate liquid flows inside these porous components, a big knowledge gap exists to fully employ them in engineering design/control and material development. First, experimental data are still lacking regarding the liquid water distribution and impacts inside CLs due to the challenge of high-resolution experimental detection in such thin layers. In reality, CLs are not flat layer. Instead, they may be ruptured as revealed by the X-ray images, making it challenging to directly measure the water profile across the CL thickness. Similar challenges exist for MPLs as well, which are ~50 μm thick. At present, most models have not been fully validated in MPLs and CLs in terms of liquid water distribution. As to the GDLs, they show highly mixed wettability, in other words, some areas where only carbon is present are highly hydrophilic whereas other areas where Teflon is also present are highly hydrophobic. This mixed-wettability property is not accounted for in most of the macroscopic models for PEM fuel cells. The pore size and local porosity distributions, as well as hydrophilicity/hydrophobicity distributions, are found to greatly influence liquid water profiles in GDLs, making it difficult to develop a reliable engineering model to fully account for all of these factors. Fig. 12 shows water accumulation, caused by spatially varying porosity and hence permeability. The fundamentals regarding the impacts of material heterogeneity can be described by the capillary pressure-driven liquid flux [265]:

$$\frac{\lambda_l\lambda_g}{\nu}K\nabla P_c(\sigma,\theta_c,\varepsilon,K,s)=\frac{\lambda_l\lambda_g}{\nu}K\left(\frac{\partial P_c}{\partial\sigma}\nabla\sigma+\frac{\partial P_c}{\partial\theta_c}\nabla\theta_c+\frac{\partial P_c}{\partial\varepsilon}\nabla\varepsilon+\frac{\partial P_c}{\partial K}\nabla K+\frac{\partial P_c}{\partial s}\nabla s\right) \quad (4)$$

In general, the material heterogeneity, including the spatially varying contact angle, surface tension, or permeability, influences the liquid flux and hence water distribution. In material fabrication, different PTFE-drying methods (i.e. the vacuum and air drying) will lead to spatial variation of the PTFE distribution and hence that of contact angle, which affects water profiles [269]. The air dried GDL yields a high PTFE loading near the GDL

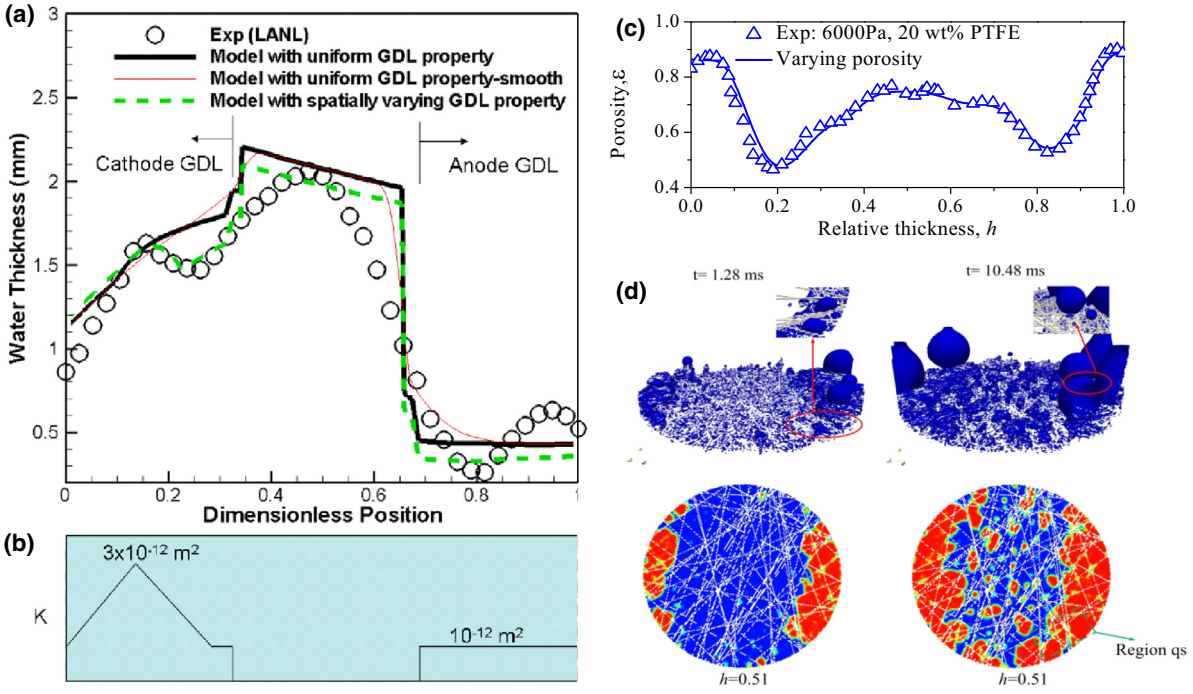

FIGURE 12

(a) Liquid water profiles in GDLs from the high resolution neutron radiography data and model predictions [183,265]; (b) Varying GDL permeability used in the (a) study; (c) Local GDL porosity detected by X-ray radiography [313] and (d) 3D iso-surface of water phase fraction and 2D water contour for fiber contact angle $\theta = 109°$, 20 wt% PTFE, and pressure difference $\Delta p = 6000$ Pa [314].

surface, reducing water imbibition into the GDL. Eq. (4) also applies to the scenario of GDL under-land compression, which reduces local porosity and permeability. In short, elucidating the fundamentals of two-phase flow is essential to the material development and fabrication, which include the mean pore size; porosity; surface wettability; their spatial distribution; fuel cell design parameters, such as thickness and land compression; and operational control.

Two-phase flow in GFCs

Gas flow channels (GFCs) supply and distribute gaseous reactants, and remove byproduct water. They are typically embedded in the BPs, thus the GFC dimension, specifically the depth, limits the minimal BP thickness. A small GFC may raise multiple concerns, including a large pressure drop hence high pumping power consumption, liquid blockage, and GDL intrusion. Several GFC designs have been proposed, including parallel, serpentine, pin-type, interdigitated, and porous media flow fields. The design objective is to evenly distribute the gaseous reactants and effectively remove water with minimal demand on pumping power. Though CFD software are commercially available to aid the GFC design and predict gas flows, a few features unique to PEM fuel cells need to be incorporated in order to capture the realistic operation, including (1) the mass loss/gain due to electrochemical reactions and species transport [270]; (2) the roughness of GDL surfaces [271]; and (3) the GDL intrusion into the channel space. The mass loss/gain will significantly influence the anode flow rate. For example, a pure hydrogen flow will reduce its flow rate by ~80% for a stochastic ratio of 1.2 operation [78]. The GDL roughness/intrusion alters the flow cross-section area, which is a cause to flow maldistribution among parallel GFCs [272–274].

Another challenge is liquid water removal, including droplets at the GDL/GFC surface, liquid flow at hydrophilic channel walls, and two-phase flow behaviors with GFC heterogeneity. At present, no effective models are available to predict two-phase flow in GFCs in a fuel cell. Most existing models are either empirical or computationally intensive (e.g. volume of fluids and LBM methods). Two-phase flow behavior consists of several subprocesses: (1) transport from the CL to the GDL/GFC interface via capillary action; (2) removal at the GDL/GFC interface via detachment or evaporation; (3) transport through the GFC in form of films, droplets, and/or vapor; and (4) liquid accumulation due to GFC heterogeneity, e.g. at the GFC-manifold joint. The growth and detachment of water droplets are influenced by two factors: the operating conditions and the physical (e.g., surface roughness) and chemical (e.g., wettability) material characteristics of the GDL surface (e.g. in terms of the hydrophilic/hydrophobic properties). Mechanics models have been developed to understand the droplet deformation and detachment [274–278]. In particular, Chen and coworkers developed force balance models to predict the onset of instability leading to removal of water droplets and droplet deformation. To prevent formation of large droplets that effectively block the channel flow, a fast gas flow rate and a thin GFC are helpful. Modeling liquid flow in GFCs is another challenge given the various patterns that may be encountered, including annulus, wavy annulus, wavy, and slug flows, see Fig. 13 [279–287]. The flow pattern greatly influences the gas pressure drop, thus parallel GFCs, subject to different patterns, will cause flow maldistribution [204,331]. A few approaches were attempted to formulate a two-phase flow model in GFCs, including the VOF [282], LBM [283], two-fluid approach [9,284], and mixed multiphase (M2) descrip-

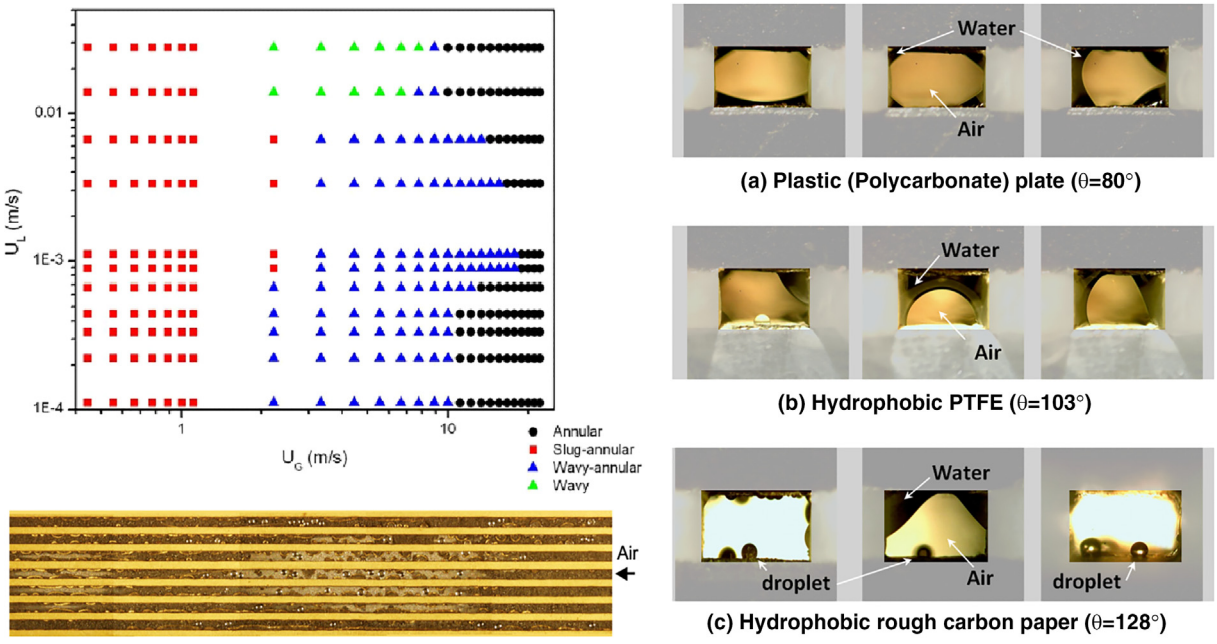

FIGURE 13

Two-phase pattern in PEM fuel cell GFCs (left) and liquid water location in microchannels of various surface properties (right) [279–285,324–325].

tion [48,291]. The former two are usually computationally expensive, making it difficult to incorporate with other components of fuel cells. Analytical solutions were developed from the two-fluid and M2 models, showing a good agreement with experimental data [48,285]. Again, fundamentals critical to GFC design/control are needed to understand water buildup, impacts of channel heterogeneity,e.g. expansion to a manifold [286], and flow maldistribution, and their dependence on the GFC surface properties, including roughness and wettability [280,285,294].

A novel design of porous media GFCs was proposed by Wang [9,10] to better manage the transport of heat, electron, and water and two-phase flow and enable flexible GFC design, including the channel dimension (e.g. the channel/rib width, thickness, and length), structure (e.g. random and regular structures), novel fabrication (e.g. highlyporous media manufacturing), and material selection (e.g. carbon, Ti, and coating materials). This type of design was adopted in the cathode 3-D fine mesh porous media flow filed of the Toyota Mirai FCVs [54], featured by carbon-coated Ti porous media of 0.3 mm in thickness. Similar 3D mesh porous media flow fields were numerally investigated and shown to significantly decrease the concentration loss [287]. Metal foam and cellular foam porous media flow fields were also studied, showing nearly uniform current density and temperature distributions [288] and higher cell performance [289], respectively. However, porous media flow fields have a concern of raising the pressure drop and hence pumping power, and liquid water accumulation. The ratio of the pumping power demanded for the cathode flow to the electric power produced by fuel cell, $\beta_{pumping}$, is estimated by [10]:

$$\beta_{pumping} \approx \frac{A_m v \rho L I}{16 V_{cell} A_c} \left(\frac{\xi_c}{F C_{O2}}\right)^2 \frac{1}{K} \quad (5)$$

where the flow field permeability (K) and cross-section area (A_c) can be designed to achieve the pumping power target.

Dynamic control and cold start

Dynamic operation is of paramount importance to fuel cell applications, such as portables, FCVs, and drones. Fuel cell dynamics consist of various multi-timescale processes, including the electrochemical double-layer dynamics (with a time constant of $\tau_{dl} = \delta_{CL}^2 aC(1/\kappa + 1/\sigma)$ oxygen diffusion ($\tau_D = \delta_{GCL}^2 / D_g^{eff}$), membrane hydration ($\tau_m = \frac{\rho \delta_m \Delta\lambda}{EW} / \frac{I}{3F}$) [248,298–299], phase change [292–301], and liquid drainage [48,302–303]. The former two take place fairly fast with a time constant less than 0.1 s. Hydration of Nafion® membrane takes more than 1 s due to its water uptake capability. The time constants of phase change and liquid drainage vary, dependent on the specific process. The intrinsic multi-timescale phenomena lead to overshoot or undershoot in the output voltage [290] and major power loss [248]. Material properties, including species diffusivities, thermal conductivities, porosity, and membrane water uptake, and component design greatly impact fuel cell dynamics. Specially, a thin membrane and GDL have a rapid membrane hydration, anode rehydration, and oxygen diffusion.

Another important dynamic operation is cold-start, referred as start up from a freezing point, in which water product freezes and accumulates in the cathode electrode, as revealed by neutron radiography (Fig. 14(a)) and by SEM image (Fig. 14(b)). In practice, the capability to cold-start is determined by two competing processes, namely the ice accumulation in the cathode CL and fuel cell temperature increase, as a result of the water/heat co-production by the fuel cell. For cold-start failure, additional action needs to be taken to either dry out the CL's ice or externally heat fuel cell up to overcome the 0 °C barrier. In this regard, one can define a control parameter as the ratio of the two-time constants of fuel cell heating and ice accumulation [181]:

$$\beta_2 = \frac{\tau_{T,1}}{\tau_{s_{ice}}} \quad (6)$$

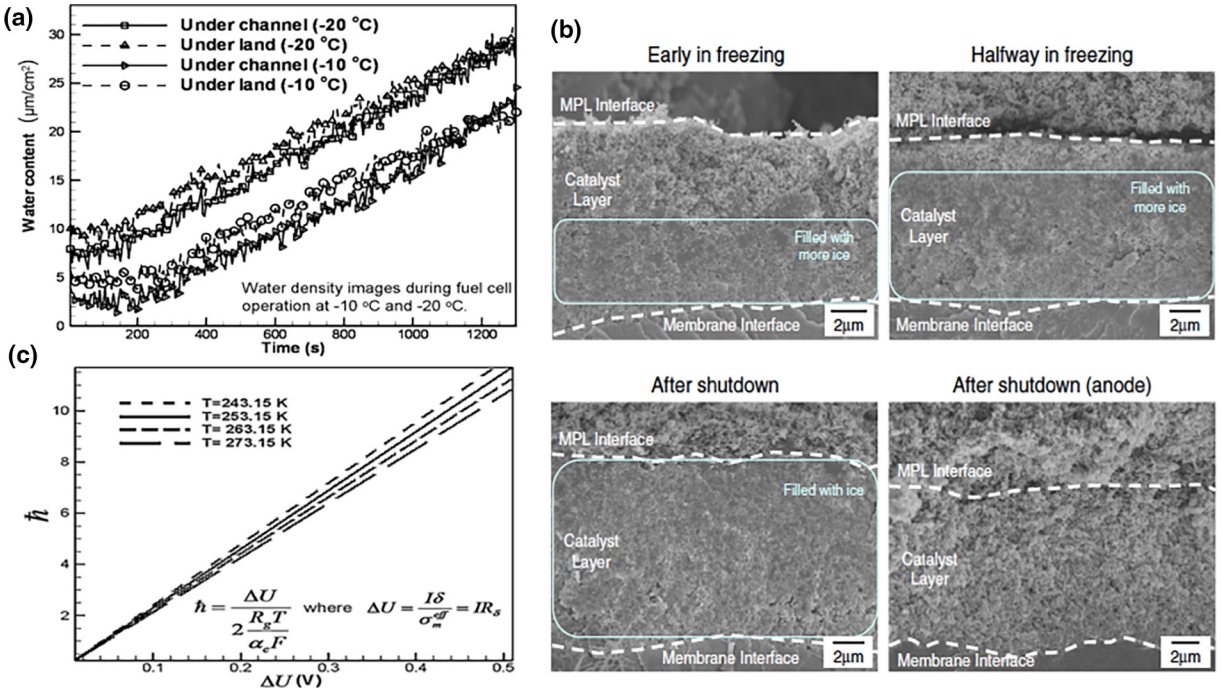

FIGURE 14

(a) Ice content evolution during fuel cell operation at two subfreezing temperatures −10 and −20 °C obtained from neutron radiography [317]; (b) Cryo-SEM images of cross-sections of a CL under two currents [318]; (c) Non-uniformity of the ORR reaction under subfreezing temperatures [253].

where $\tau_{s_{ice}} = \frac{2F\delta_{CL}}{(1+2\alpha)I}\left(\frac{\rho_m \varepsilon_m (14-\lambda_0)}{EW} + \frac{\varepsilon_{CL}\rho_{ice}}{M^w}\right)$ and $\tau_{T,1} = \frac{\rho_{BP}Cp_{BP}\delta_{BP}}{I(E_o - Vcell)}(273.15 - T_o)$.

In unassisted cold-start, β_2 needs to be less than 1 in order for a successful startup. This can be achieved through fuel cell design and material selection, e.g. a large CL thickness (δ_{CL}), ionomer fraction (ε_m), or porosity (ε_{CL}) or small BP thickness (δ_{BP}) and thermal capacity ($\rho_{BP}Cp_{BP}$). In practice, ice formation is non-uniform throughout the CL, as indicated by a reaction non-uniformity factor ħ, see Fig. 14(c) [253]. For electrode design, the coulombs of charge Q_c transferred in PEM fuel cells before the output voltage drops to 0.0 V was introduced as a parameter to measure the fuel cell cold-start capability. The CL composition, startup temperature, membrane hydration, and CL thickness all affect this parameter, see Fig. 15(a). In addition, high-resolution neutron radiography indicated most ice forms in the cathode side of the

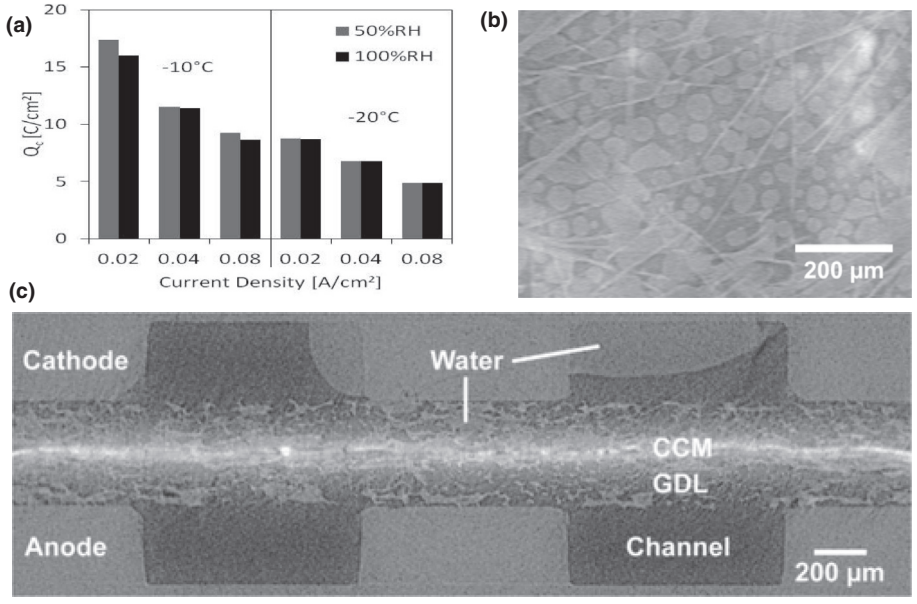

FIGURE 15

(a) Coulombs transferred before voltage failure [296]; (b) Horizontal slice of CL for freeze start (−20 °C, 0.3 A cm^{-2}). Small droplets of water are visible on the surface of the CL; (c) Cross-section through the cell of freeze start (−10 °C, 0.1 A cm^{-2}), showing water in the GDL and channel [319].

MEA [296]. Two ice morphologies were proposed, including ice nucleation and film, which have distinct impacts on the ORR reaction [253]. It was also indicated that the impacts of ice formation, including increased surface coverage and oxygen transport resistance, are analogous to those of insoluble Li oxides on Li-air battery cathode performance, thus similar analysis is applicable [297–307]. The U.S. DOE target is unassisted cold-start from −30 °C, which was achieved by 2015 [19]. A recent review on cold start was provided by Wan et al. [300], Amamou et al. [301], and Luo and Jiao [302].

Another critical issue related to cold start is degradation of components, such as GDLs and CLs [303]. In GDLs, the freezing/thaw cycles may reduce their hydrophobicity and break fiber linkage [304]. In CLs, cold starts may reduce the ECSA. In addition, supercooled water under subfreezing condition was observed to flow to GDL and GFC, as shown in Fig. 15 (b) and (c). Sabawa and Bandarenka [305] investigated degradation mechanisms during freeze-cycles using electrochemical impedance spectrum (EIS), indicating that the water content on the anode and cathode plays an important role in the degradation.

Summary and concluding remarks

In this review, the latest status of PEM fuel cell technology and issues related to materials, design, and balance of plant (BOP) are reviewed; and the needs on fundamental research are discussed. To date, more than 4000 commercial FCVs and 30 FCBs have been deployed worldwide. Three FCBs were rated at the technical readiness stage of full-scale validation in realistic environments and have served millions of passengers in the United States; moreover, a FCB by 2016 almost met the 25,000-h ultimate goal set by the US DOE. In 2017, Toyota started to sell its first commercial Mirai FCV, at a price less than $59,000 with a fuel cell stack having 153 HP and 3.1 kW/L and 2 kW/kg capacity, and a 122.4L 700 bar hydrogen tank for approximate 300 miles range [314].

Primary barriers, including durability, cost, and hydrogen infrastructure availability, to the world-wide commercialization of PEM fuel cell technology are explained. Significant progress toward commercialization has been made in the last three decades or so, but challenges remain, in particular with respect to durability and cost. DOE's target of durability lifetime is greater than 5000 h by 2025 and ultimately 8000 h for FCVs, and 25,000 h for FCBs. So far, the Toyota Mirai has achieved 3000 h in the real-world driving testing but failed the AST protocol testing developed by the DOE. DOE's target of cost is $45/kW in 2025 and ultimately $30/kW for FCVs. The current cost for a FCB is about 1 million dollars at high volume production. At present, there are over 30 and 60 hydrogen gas stations in the U.S., mostly in the state of California, and Germany, respectively. More than 100 hydrogen gas stations are currently under planning for the next five years. On the gas station side, hydrogen compressors currently cost about $700,000 for 35 kg/h of capacity and fueling nozzles cost approximately $7000 each. Compressed hydrogen is transported in tube trailers, typically under 200–500 bar, with a 250–1000 kg hydrogen payload. Liquefied hydrogen is transported using multi-layer vacuum insulated dewars capable of over 4000-kg payloads.

Bipolar plates (BPs) contribute a major weight and volume (~70–90%) of a PEM fuel cell. The gas flow channel (GFC) dimensions limit further reduction in the BP weight/volume. The porous media flow field design enables a flexible GFC design and better transport of reactants, heat, and two-phase flow, which is adopted in the cathode of the Toyota Mirai FCV system. The size of the hydrogen storage tank determines the energy capability of a fuel cell system, and the current technology in FCV/FCBs equips with compressed hydrogen around 70–80 MPa. The BOP adds another portion of weight and volume to the FCV system, which can be reduced by low-humidity operation, advanced control, unassisted cold-start capability, and efficient cooling technology.

Elucidating fundamentals of PEM fuel cells is vitally important to the technology advancement, barrier breakthroughs, and optimal design. The role of and the needs for fundamental research, as well as the associated challenges, are summarized and discussed in this review. Specially, for membrane and catalyst layer, both require significant further research in order to identify and develop alternative cost-effective materials. MEAs with better degradation resistance and low Pt loading are critical to achieving the DOE cost and durability or lifetime targets. For GDLs and MPLs, fundamental understanding of liquid–water behaviors in these components is required, in particular on the effects of their micro structure and mixed wettability. For BPs and GFCs, fundamental knowledge of liquid droplet removal at the GDL/GFC interfaces and two-phase flow in micro-channels of varying surface roughness and wettability is challenging to acquire, but such knowledge is in urgent need in order to optimize GFC design that can ensure efficient water removal and reactant supply and avoid flow maldistribution and thus maintain high fuel-cell performance.

Acknowledgment

We gratefully acknowledge the support of the National Science Foundation, USA (CBET-1336873) and our industry sponsors on this study. YW also thanks Sung Chan Cho, Hao Yuan, and James Lewis for their assistance in preparing the paper.

Appendix A. Supplementary data

Supplementary data to this article can be found online at https://doi.org/10.1016/j.mattod.2019.06.005.

References

[1] F.T. Bacon, Electrochim. Acta 14 (7) (1969) 569–585.
[2] A.J. Appleby, E.B. Yeager, Energy 11 (1–2) (1986) 137–152.
[3] I.D. Raistrick, Modified gas diffusion electrode for proton exchange membrane fuel cells, in: Proceedings of the Symposium on Diaphragms, Separators, and Ion-Exchange Membranes (Vol. 86), 1986, p. 172.
[4] I.D. Raistrick, U.S. Patent No. 4,876,115. Washington, DC: U.S. Patent and Trademark Office, 1989.
[5] I. Raistrick, Electrode Assembly for Use in a Solid Polymer Electrolyte Fuel Cell. U.S. Patent No. 4,876,115, 1989.
[6] M.S. Wilson, U.S. Patent No. 5,211,984. Washington, DC: U.S. Patent and Trademark Office, 1993.
[7] M.S. Wilson, UU.S. Patent No. 5,234,777. Washington, DC: U.S. Patent and Trademark Office, 1993.
[8] S. Gottesfeld, J. Pafford, J. Electrochem. Soc. 135 (10) (1988) 2651–2652.
[9] Y. Wang, J. Electrochem. Soc. 156 (10) (2009) B1134–B1141.
[10] Y. Wang, J. Electrochem. Soc. 156 (10) (2009) B1124–B1133.

[11] S. Satyapal, Hydrogen and fuel cells porgram overview, US Department of Energy Annual Merit Review, June 13–15, 2018, in Washington, D.C., 2018.
[12] Y. Wang et al., Appl. Energy 88 (4) (2011) 981–1007.
[13] C. Herwerth, C.Chiang, A. Ko, S. Matsuyama, S.B. Choi, M. Mirmirani, A. Koschany, Development of a small long endurance hybrid PEM fuel cell powered UAV (No. 2007-01-3930). SAE Technical Paper, 2007.
[14] N. Lapeña-Rey, J. Mosquera, E. Bataller, F. Ortí, The Boeing fuel cell demonstrator airplane (No. 2007-01-3906). SAE Technical Paper, 2007.
[15] D. Papageorgopoulos, Fuel Cells R&D Overview, Annual Merit Review and Peer Evaluation Meeting Washington DC. June 13–15, 2018, 2018.
[16] R. Borup, R. Mukundan, K. More, K. Neyerlin, A. Weber, D. Myers, R. Ahluwalia, PEM fuel cell catalyst layer (MEA) Architectures. The Electrochemical Society Meeting, 2018.
[17] R.L. Borup, K.L. More, D.J. Myers, FC-PAD: Fuel Cell Performance and Durability Consortium Update to USCAR Analysis of Toyota Mirai Components Provided by USCAR (No. LA-UR-18-24454). Los Alamos National Lab. (LANL), Los Alamos, NM (United States), 2018.
[18] L. Eudy, Technology Validation: Fuel Cell Bus Evaluations (No. NREL/PR-5400-66177), National Renewable Energy Lab. (NREL), Golden, CO (United States), 2018.
[19] U.S. Department of Energy, DOE Technical Targets for Fuel Cell Systems and Stacks for Transportation Applications, Internet Publication, 2015. <https://www.energy.gov/eere/fuelcells/doe-technical-targets-fuel-cell-systems-and-stacks-transportation-applications>.
[20] D. Carter, M. Ryan, J. Wing, The fuel cell industry review 2012. E2nd, London, 2012.
[21] D. Carter, J. Wing, The fuel cell industry review 2013. E3rd, London, 2013.
[22] D. Hart, F. Lehner, R. Rose, J. Lewis, M. Klippenstein, The Fuel Cell Industry Review 2017, E4tech, London, 2017.
[23] K.A. Adamson, 4th Energy Wave Fuel Cell and Hydrogen Annual Review 2015, 2015.
[24] K.A. Adamson, 4th Energy Wave Fuel Cell and Hydrogen Annual Review 2016, 2016.
[25] S. Curtin, J. Gangi, Fuel Cell Technologies Market Report 2015, Fuel Cell and Hydrogen Energy Association, Washington, 2015.
[26] S. Curtin, J. Gangi, Fuel Cell Technologies Market Report 2016, Fuel Cell and Hydrogen Energy Association, Washington, 2016.
[27] Intelligent Energy, Internet Publication. <https://www.intelligent-energy.com>, 2018.
[28] Intelligent Energy, Intelligent Energy leads UAV fuel cell power market with launch of 2.4 kW module <https://www.intelligent-energy.com/news-and-events>, Internet Publication, 2019.
[29] MyFC, Internet Publication. <https://myfcpower.com>, 2017.
[30] MyFC Unveils Thinnest Fuel Cell at CES, Wins Good Design Award. Fuel Cells Bull., 2017(1) (2017) 7-7.
[31] My H2. LIVE.Hydrogen reaches Leverkusen, Internet Publication, 2019. <https://h2.live/en/news/682>.
[32] MyFC, MyFC gets repeat order from Japan <https://myfcpower.com/cision/news/A643E24AD1391389>, Internet Publication, 2019.
[33] EZelleron Inc. Kraftwerk-highly-innovative-portable-power-plant. Internet Publication. <www.kickstarter.com/projects/ezelleron/kraftwerk-highly-innovative-portable-power-plant/updates>, 2015.
[34] Aquafairy Corporation, Internet Publication. <http://www.aquafairy.co.jp/index.html>, 2006.
[35] SerEnergy A/S, 2018. Internet Publication. <https://serenergy.com/about-us/>.
[36] Fuell Cell Bulletin, Fuel Cells Bull 2013 (4) (2013). 7-7.
[37] Horizon Fuel Cell Technologies, Internet Publication. <https://www.horizonfuelcell.com>, 2013.
[38] J.N. Das, Fuel Cell Technologies for Defence Applications. In Energy Engineering, Springer, Singapore, 2017, pp. 9–18.
[39] Fuel Cell Bulletin, Fuel Cells Bull 2015 (7) (2015). 1-1.
[40] Fuel Cell Bulletin, Fuel Cells Bull 3 (2015). 10-10.
[41] Protonex, 2018. Internet Publication. <http://www.protonex.com>.
[42] Ballard Power Systems. Internet Publication. <http://www.ballard.com>, 2019.
[43] HES Energy Systems, 2009. Internet Publication. <https://www.hes.sg>.
[44] D. Hart, F. Lehner, R. Rose, J. Lewis, M. Klippenstein, The Fuel Cell Industry Review 2015, E4tech, London, 2015.
[45] D. Hart, F. Lehner, R. Rose, J. Lewis, The Fuel Cell Industry Review 2016, E4tech, London, 2016.
[46] UltraCell Internet Publication, <http://www.ultracell-llc.com>, 2016.
[47] J. Stumper, C. Stone, J. Power Sources 176 (2) (2008) 468–476.
[48] Y. Wang, S. Basu, C.Y. Wang, J. Power Sources 179 (2) (2008) 603–617.
[49] U.S. Department of Energy,. Internet Publication <https://www.energy.gov/eere/fuelcells/fuel-cell-technologies-office>, 2017.
[50] H. Greimel, Honda, GM Set Targets for 2020 Fuel Cell Vehicle, Internet Publication, 2016. <https://www.autonews.com/article/20160314/OEM05/303149972/honda-gm-set-targets-for-2020-fuel-cell-vehicle>.
[51] California Fuel Cell Partnership, LAX Hydrogen Station Opens -#39, Internet Publication, 2018. <https://cafcp.org/blog/lax-hydrogen-station-opens-39>..
[52] Ministry of Economy, Trade and Industry, Compilation of the Revised Version of the Strategic Roadmap of Hydrogen and Fuel Cells, Internet Publication, 2016. <http://www.meti.go.jp/english/press/2016/0322_05.html>.
[53] Y. Nonobe, IEEJ Trans. Electr. Electron. Eng. 12 (1) (2017) 5–9.
[54] T. Yoshida, K. Kojima, Electrochem. Soc. Interface 24 (2) (2015) 45–49.
[55] American Honda Motor Co., Inc., Internet Publication. <https://automobiles.honda.com/clarity-electric>, 2017.
[56] Hyundai Motor America, Nexo. The world's only fuel-cell SUV <https://www.hyundaiusa.com/tucsonfuelcell/index.aspx>, Internet Publication, 2017.
[57] GM Heritage Center, Internet Publication. <https://www.gmheritagecenter.com/featured/Fuel_Cell_Vehicles.html>, 2017.
[58] GM Authority, Internet Publication. <http://gmauthority.com/blog/gm/chevrolet/colorado/chevrolet-colorado-zh2/>, 2017.
[59] Mercedes-Benz, Internet Publication. <https://www.mercedes-benz.com/en/mercedes-benz/vehicles/passenger-cars/glc/the-new-glc-f-cell/>, 2018.
[60] T.J. Leo, J.A. Durango, E. Navarro, Energy 35 (2) (2010) 1164–1171.
[61] J. Hermans, MRS Energy Sustain. 4 (2017) E1, https://doi.org/10.1557/mre.2017.2.
[62] Barnard Microsystems, Internet Publication. <http://www.barnardmicrosystems.com/UAV/milestones/fuel_cell.html>, 2014.
[63] T.H. Bradley et al., J. Aircr. 46 (6) (2009) 1945–1956.
[64] K. Swider-Lyons, Ion Tiger Fuel Cell Powered UAV, Internet Publication, 2013. <https://www.nrl.navy.mil/lasr/content/ion-tiger-fuel-cell-powered-uav>.
[65] New Atlas Team, World's First Commercial Fuel Cell Unmanned Aerial System, Internet Publication, 2009. <https://newatlas.com/worlds-first-commercial-fuel-cell-unmanned-aerial-system/12453/>.
[66] K. Kang et al., Fuel Cells 14 (5) (2014) 694–700.
[67] T. Wankewycz, H3 Dynamics Launches HYWINGS, a Fuel Cell Electric UAV Capable of 10h Flights, Internet Publications, 2016. <https://www.businesswire.com/news/home/20161114005635/en/H3-Dynamics-Launches-HYWINGS-Fuel-Cell-Electric.
[68] G. McAree, Ballard's Protonex Subsidiary Receives First Order for Fuel Cell System to Power Commercial, Inter Publication, 2017. <http://ballard.com/modules-display/news-releases/2017/06/14/ballard-s-protonex-subsidiary-receives-first-order-for-fuel-cell-system-to-power-commercial-uavs>.
[69] Fuel Cell Bulletin, Fuel Cells Bulletin 2011 (9) (2011) 4–5.
[70] N. Lapeña-Rey et al., J. Aircr. 47 (6) (2010) 1825–1835.
[71] G. Renouard-Vallet et al., Chem. Eng. Res. Des. 90 (1) (2012) 3–10.
[72] P. Ridden, Hydrogen Fuel Cell Four-Seater Passenger Plane Takes to the Air, Internet Publication, 2016. <http://newatlas.com/hy4-hydrogen-fuel-cell-passenger-plane-test-flight/45687/>.
[73] S. Eelman, I.D.P. de Poza, T. Krieg, Fuel cell APU'S in commercial aircraft an assessment of SOFC and PEMFC concepts, 24th international congress of the Aeronautical sciences, ICAS 2004, 2004.
[74] D.B. Curgus, K. Munoz-Ramos, J.W. Pratt, A.A. Akhil, L.E. Klebanoff, B.L. Schenkman, Proton Exchange Membrane Fuel Cells for Electrical Power Generation On-Board Commercial Airplanes (No. SAND2011-3119), Sandia National Laboratories, 2011.
[75] K.A. Friedrich et al., ECS Trans. 25 (1) (2009) 193–202.
[76] S.J. Peighambardoust, S. Rowshanzamir, M. Amjadi, Int. J. Hydrogen Energy 35 (17) (2010) 9349–9384.
[77] F.C. Handbook, EG&G Technical Services. Inc., Albuquerque, NM, DOE/NETL-2004/1206, 1–10, 2004.
[78] Y. Wang, K.S. Chen, S.C. Cho, PEM Fuel Cells: Thermal and Water Management Fundamentals, Momentum Press, 2013.
[79] J. Larminie, A. Dicks, M.S. McDonald, Fuel cell systems explained vol. 2 (2003) 207–225.
[80] M. Eikerling, A. Kulikovsky, Polymer Electrolyte Fuel Cells: Physical Principles of Materials and Operation, CRC Press, 2014.
[81] C. Kunusch, P. Puleston, M. Mayosky, Sliding-Mode Control of PEM Fuel Cells, Springer Science & Business Media, 2012.
[82] C.K. Jin, M.G. Jung, C.G. Kang, Fuel Cells 14 (4) (2014) 551–560.
[83] E. Planes, L. Flandin, N. Alberola, Energy Procedia 20 (2012) 311–323.
[84] O.A. Alo et al., Procedia Manuf. 7 (2017) 395–401.
[85] A. Hermann, T. Chaudhuri, P. Spagnol, Int. J. Hydrogen Energy 30 (12) (2005) 1297–1302.

[86] M. Kim, J.W. Lim, K.H. Kim, Compos. Struct. 96 (2013) 569–575.
[87] N.A.M. Radzuan et al., Composites Part B: Eng. 110 (2017) 153–160.
[88] A. Adloo et al., Renewable Energy 99 (2016) 867–874.
[89] P.L. Hentall et al., J. Power Sources 80 (1–2) (1999) 235–241.
[90] H. Tawfik, Y. Hung, D. Mahajan, J. Power Sources 163 (2) (2007) 755–767.
[91] N.B. Huang et al., Results Phys. 6 (2016) 730–736.
[92] Z. Li et al., Int. J. Hydrogen Energy 39 (16) (2014) 8421–8430.
[93] J. Barranco et al., Int. J. Hydrogen Energy 35 (20) (2010) 11489–11498.
[94] M.M. Sisan et al., J. Alloys Compd. 613 (2014) 288–291.
[95] P. Chen et al., Int. J. Hydrogen Energy 42 (17) (2017) 12593–12600.
[96] S.J. Lee, C.H. Huang, Y.P. Chen, J. Mater. Process. Technol. 140 (1–3) (2003) 688–693.
[97] M.A. Deyab, J. Power Sources 268 (2014) 50–55.
[98] J.R. Mawdsley et al., J. Power Sources 231 (2013) 106–112.
[99] D.P. Davies et al., J. Power Sources 86 (1–2) (2000) 237–242.
[100] H. Wang, M.A. Sweikart, J.A. Turner, J. Power Sources 115 (2) (2003) 243–251.
[101] R.A. Antunes et al., Int. J. Hydrogen Energy 35 (8) (2010) 3632–3647.
[102] N.F. Asri et al., Int. J. Hydrogen Energy 42 (14) (2017) 9135–9148.
[103] A.C. Stoot et al., J. Power Sources 293 (2015) 846–851.
[104] N.W. Pu et al., J. Power Sources 282 (2015) 248–256.
[105] K. Lin et al., Int. J. Hydrogen Energy 39 (36) (2014) 21470–21479.
[106] Y. Zhao et al., Int. J. Hydrogen Energy 41 (2) (2016) 1142–1150.
[107] M. Omrani et al., Int. J. Hydrogen Energy 37 (19) (2012) 14676–14686.
[108] S.H. Lee et al., Thin Solid Films 529 (2013) 374–379.
[109] D. Zhang et al., Int. J. Hydrogen Energy 35 (8) (2010) 3721–3726.
[110] D. Zhang et al., Int. J. Hydrogen Energy 36 (15) (2011) 9155–9161.
[111] K. Feng et al., J. Power Sources 195 (19) (2010) 6798–6804.
[112] M. Herdlitschka, Mercedes-Benz F-Cell: Market Launch of the World's First Electric Vehicle Featuring Fuel Cell and Plug-in Hybrid Technology, Internet Publication, 2018. <https://media.daimler.com/marsMediaSite/en/instance/ko/Mercedes-Benz-GLC-F-CELL-Market-launch-of-the-worlds-first-electric-vehicle-featuring-fuel-cell-and-plug-in-hybrid-technology.xhtml?oid=41813012>.
[113] P. Yi et al., J. Power Sources 230 (2013) 25–31.
[114] P. Yi et al., Int. J. Hydrogen Energy 38 (3) (2013) 1535–1543.
[115] H. Sun et al., Thin Solid Films 528 (2013) 199–204.
[116] F. Bi et al., J. Power Sources 314 (2016) 58–65.
[117] D.K. Merl, P. Panjan, M. Panjan, M. Čekada, Plasma Processes Polym. 4 (S1) (2007) S613–S617.
[118] S.M. Haile, Acta Mater. 51 (19) (2003) 5981–6000.
[119] S. Banerjee, Handbook of specialty fluorinated polymers: Preparation, Properties, and Applications, William Andrew, 2015.
[120] J. Roziere, D.J. Jones, Annu. Rev. Mater. Res. 33 (1) (2003) 503–555.
[121] F. Bauer, S. Denneler, M. Willert-Porada, J. Polym. Sci. Part B: Polym. Phys. 43 (7) (2005) 786–795.
[122] R. Devanathan, Energy Environ. Sci. 1 (1) (2008) 101–119.
[123] D. Jones, Mater. Matters 10 (3) (2015) 42–43.
[124] B. Kienitz et al., ECS Trans. 41 (1) (2011) 1521–1530.
[125] N.H. Jalani, K. Dunn, R. Datta, Electrochim. Acta 51 (3) (2005) 553–560.
[126] S.Y. Chen, C.C. Han, C.H. Tsai, J. Huang, Y.W. Chen-Yang, J. Power Sources 171 (2) (2007) 363–372.
[127] Y. Devrim et al., Int. J. Energy Res. 37 (5) (2013) 435–442.
[128] Y. Devrim, H. Devrim, Int. J. Hydrogen Energy 40 (24) (2015) 7870–7878.
[129] K.R. Yoon et al., Adv. Funct. Mater. 29 (3) (2019) 1806929.
[130] E. Quartarone, S. Angioni, P. Mustarelli, Materials 10 (7) (2017) 687.
[131] D. Papageorgopoulos, Fuel Cells Program Area, Annual Merit Review and Peer Evaluation Meeting June 6–10, 2016, 2016.
[132] M. Yandrasits et al., J. Electrochem. Soc. 165 (6) (2018) F3261–F3270.
[133] H.K. Yasuda, General characteristics of plasma polymers, in: Plasma Polymerization, Academic Press, London, 1985, p. 355.
[134] M.M. Nasef, Chem. Rev. 114 (24) (2014) 12278–12329.
[135] J. Kerres, W. Zhang, T. Haering, J. New Mater. Electrochem. Syst. 7 (4) (2004) 299–310.
[136] F.C. Ding et al., J. Power Sources 164 (2) (2007) 488–495.
[137] C.I. Morfopoulou et al., J. Mater. Chem. A 1 (5) (2013) 1613–1622.
[138] A. Mohammad, A.M. Asiri (Eds.), Organic-Inorganic Composite Polymer Electrolyte Membranes: Preparation, Properties, and Fuel Cell Applications, Springer, 2017.
[139] M. Rezakazemi, M. Sadrzadeh, T. Mohammadi, T. Matsuura, Methods for the preparation of organic–inorganic nanocomposite polymer electrolyte membranes for fuel cells, in: Organic-Inorganic Composite Polymer Electrolyte Membranes, Springer, Cham, 2017, pp. 311–325.
[140] F. Wang et al., Science 197 (1–2) (2002) 231–242.
[141] J. Xu et al., J. Membr. Sci. 492 (2015) 505–517.
[142] E. Passalacqua et al., Electrochim. Acta 46 (6) (2001) 799–805.
[143] J. Xie et al., Electrochim. Acta 55 (24) (2010) 7404–7412.
[144] Y. Wang et al., J. Electrochem. Soc. 164 (13) (2017) F1294–F1300.
[145] S.C. Snyder et al., Appl. Spectrosc. 65 (6) (2011) 642–647.
[146] Y. Wang, X. Feng, J. Electrochem. Soc. 156 (3) (2009) B403–B409.
[147] X. Feng, Y. Wang, Electrochim. Acta 55 (15) (2010) 4579–4586.
[148] M.K. Debe, Nature 486 (7401) (2012) 43.
[149] M. Shao et al., Chem. Rev. 116 (6) (2016) 3594–3657.
[150] B. Popov, Development of Ultra-Low Doped-Pt Cathode Catalysts for PEM Fuel Cells (PHASE II), Department of Energy Hydrogen and Fuel Cells Program Review Development, 2015.
[151] J.L. Fernández, D.A. Walsh, A.J. Bard, J. Am. Chem. Soc. 127 (1) (2005) 357–365.
[152] C.R. Rao, D.C. Trivedi, Coord. Chem. Rev. 249 (5–6) (2005) 613–631.
[153] A. Reiner, F. Hajbolouri, M. Dobeli, A. Wokaun, G.G. Scherer, Co-Sputtering: A novel Platinum-Carbon Catalyst Preparation Method, 3rd European PEFC Forum, Lucerne, Poster 19, 2005.
[154] P. Pharkya, A. Alfantazi, Z. Farhat, J. Fuel Cell Sci. Technol. 2 (3) (2005) 171–178.
[155] Z.R. Ismagilov et al., Catal. Today 102 (2005) 58–66.
[156] P. Yu, M. Pemberton, P. Plasse, J. Power Sources 144 (1) (2005) 11–20.
[157] N. Travitsky, T. Ripenbein, D. Golodnitsky, V. Livhits, Y. Rosenberg, Y. Lereah, L. Brustein, E. Peled, Nanometric platinum and platinum-alloy-supported catalysts for oxygen reduction in PEM fuel cells, 3rd European PEFC forum, Lucerne, Switzerland, 2005.
[158] J. Xie et al., J Electrochem. Soc. 152 (2005) A104–A113.
[159] P. Wells et al., Preparation of Cr/Pt/C Catalysts by the Controlled Surface Modification of Pt/C using an Organometallic Precursor, 3rd European PEFC Forum, Lucerne Poster, 2005, p. 119.
[160] R.G. González-Huerta, J.A. Chávez-Carvayar, O. Solorza-Feria, J. Power Sources 153 (1) (2006) 11–17.
[161] Haug, Novel ionomers and electrode structures for improved PEMFC electrode performance at low PGM loadings, US Department of Energy Annual Merit Review, June 13–15, 2018, in Washington, D.C., 2018.
[162] P.N. Pintauro, J. Ballengee, M. Brodt, U.S. Patent No. 9,876,246, Washington, DC: U.S. Patent and Trademark Office, 2018.
[163] P. Pintauro, Fuel Cell Membrane-Electrode-Assemblies with Ultra-Low Pt Nanofiber Electrodes, US Department of Energy Annual Merit Review, June 13–15, 2018, Washington, D.C., 2018.
[164] R. Adzic, J. Zhang, Y. Mo, M. Vukmirovic, U.S. Patent No. 9,005,331. Washington, DC: U.S. Patent and Trademark Office, 2015.
[165] L. Chong et al., Science 362 (6420) (2018) 1276–1281.
[166] Z. Bai et al., Catalysts 5 (2) (2015) 747–758.
[167] G. Wu, Front. Energy 11 (3) (2017) 286–298.
[168] C.W. Bezerra et al., Electrochim. Acta 53 (15) (2008) 4937–4951.
[169] B. Wang, J. Power Sources 152 (2005) 1–15.
[170] P. Zelenay, Y. Yan, A. Wieckowski, D. Myers, K. More, P. Atanassov, et al., Advanced cathode catalysts, in: 2010 Hydrogen Program Annual Merit Review and Peer Evaluation Meeting, Washington, DC. D. Zhang, L. Duan, L. Guo, W. H. Tuan, 2010.
[171] H.T. Chung et al., Science 357 (6350) (2017) 479–484.
[172] A. Serov, K. Artyushkova, P. Atanassov, Adv. Energy Mater. 4 (10) (2014) 1301735.
[173] H. Zhang et al., Nano Energy 31 (2017) 331–350.
[174] Eisman et al., Electrochem. Soc. Proc. 86 (13) (1986) 186.
[175] K.S. Dhathathreyan, N. Rajalakshmi, Polymer electrolyte membrane fuel cell, in: S. Basu (Ed.), Recent Trends in Fuel Cell Science and Technology, Anamaya Publishers, New Delhi, 2007, pp. 40–115. doi:10.1007/978-0-387-68815-2_3.
[176] A. Chen, C. Ostrom, Chem. Rev. 115 (21) (2015) 11999–12044.
[177] X. Xie et al., Energy Environ. Sci. 5 (5) (2012) 6862–6866.
[178] N. Jha et al., Sci. Rep. 3 (2013) 2257.
[179] E. Proietti et al., Nat. Commun. 2 (2011) 416.
[180] Y. Nabae, A. Ishihara, Recent Progress in Non-precious Metal Fuel Cell Catalysts. In Nanocarbons for Energy Conversion: Supramolecular Approaches, Springer, Cham, 2019, pp. 253–276.
[181] Y. Wang, J. Electrochem. Soc. 154 (10) (2007) B1041–B1048.
[182] Y. Wang, X. Feng, J. Electrochem. Soc. 155 (12) (2008) B1289–B1295.
[183] Y. Wang, K.S. Chen, Chem. Eng. Sci. 66 (15) (2011) 3557–3567.
[184] F.Y. Zhang, S.G. Advani, A.K. Prasad, J. Power Sources 176 (1) (2008) 293–298.
[185] S. Tanaka et al., J. Power Sources 330 (2016) 273–284.
[186] A. Jayakumar et al., Materials 10 (7) (2017) 796.
[187] G. Gautier, S. Kouassi, Int. J. Energy Research 39 (1) (2015) 1–25.

[188] J. Benziger et al., J. Membr. Sci. 261 (1–2) (2005) 98–106.
[189] J.H. Nam et al., Int. J. Heat Mass Transfer 52 (11–12) (2009) 2779–2791.
[190] R.K. Phillips et al., Energy Procedia 29 (2012) 486–495.
[191] J. Che, T. Cagin, W.A. Goddard III, Nanotechnology 11 (2) (2000) 65.
[192] A.A. Balandin et al., Nano Lett. 8 (3) (2008) 902–907.
[193] M.J. Biercuk et al., Appl. Phys. Lett. 80 (15) (2002) 2767–2769.
[194] S. Stankovich et al., Nature 442 (7100) (2006) 282.
[195] M. Suzuki, H. Shimanuki, T. Katagiri, Y. Kusano, U.S. Patent No. 6,953,635. Washington, DC: U.S. Patent and Trademark Office, 2005.
[196] H.Y. Kim. U.S. Patent No. 8,317,167. Washington, DC: U.S. Patent and Trademark Office, 2012.
[197] D. Chen, W. Li, H. Peng, J. Power Sources 180 (1) (2008) 461–467.
[198] A. Dicks, D.A.J. Rand, Fuel Cell Systems Explained, Wiley, 2018.
[199] U.S. Department of Energy. Office of Energy Efficiency and Renewable Energy (EERE), Funding Opportunity Announcement (FOA) Number: DE-FOA-0002022), 2019.
[200] D.J. Durbin, C. Malardier-Jugroot, Int. J. Hydrogen Energy 38 (34) (2013) 14595–14617.
[201] U.S. Department of Energy, Hydrogen Delivery Scenario Analysis Model, Internet Publication, 2010. <https://hdsam.es.anl.gov/index.php?content=hdsam>.
[202] G.W. Crabtree, M.S. Dresselhaus, M.V. Buchanan, Phys. Today 57 (12) (2004) 39–44.
[203] T. Umegaki et al., Int. J. Hydrogen Energy 34 (5) (2009) 2303–2311.
[204] D.A. Masten, A.B. Bosco, in: W. Vielstich, A. Lamm, H.A. Gasteiger (Eds.), Handbook of Fuel Cells Wiley, 2003: vol. 4, chapter 53, p. 714.
[205] J. Hu et al., Electrochem. Commun. 11 (12) (2009) 2324–2327.
[206] K. Pourzare, Y. Mansourpanah, S. Farhadi, Biofuel Res. J. 3 (4) (2016) 496–513.
[207] M. Yandrasits et al., Electrochem. Soc. Interface 26 (1) (2017) 49–53.
[208] G. Lakshminarayana, M. Nogami, Solid State Ionics 181 (15–16) (2010) 760–766.
[209] G. Lakshminarayana, M. Nogami, Electrochim. Acta 55 (3) (2010) 1160–1168.
[210] S.Y. Lee et al., J. Am. Chem. Soc. 132 (28) (2010) 9764–9773.
[211] T. Yasuda et al., ACS Appl. Mater. Interfaces 4 (3) (2012) 1783–1790.
[212] J. Mališ et al., Int. J. Hydrogen Energy 38 (11) (2013) 4697–4704.
[213] E. Van de Ven et al., J. Power Sources 222 (2013) 202–209.
[214] P.R. Jothi, S. Dharmalingam, J. Membr. Sci. 450 (2014) 389–396.
[215] J. Hao et al., J. Energy Chem. 24 (2) (2015) 199–206.
[216] H. Zarrin et al., J. Phys. Chem. C 115 (42) (2011) 20774–20781.
[217] Y. He et al., J. Mater. Chem. A 2 (25) (2014) 9548–9558.
[218] R. Kumar, M. Mamlouk, K. Scott, RSC Adv. 4 (2) (2014) 617–623.
[219] T. Yuan et al., Electrochim. Acta 117 (2014) 393–397.
[220] H. Beydaghi et al., RSC Adv. 5 (90) (2015) 74054–74064.
[221] G. He et al., Chem. Commun. 52 (10) (2016) 2173–2176.
[222] Y. Kim et al., J. Mater. Chem. A 3 (15) (2015) 8148–8155.
[223] L.S. Wang et al., J. Membr. Sci. 492 (2015) 58–66.
[224] S.C. Tsang et al., Nature 372 (6502) (1994) 159.
[225] D.J. Hornbaker et al., Science 295 (5556) (2002) 828–831.
[226] K. Koga et al., Nature 412 (6849) (2001) 802.
[227] D.J. Mann, M.D. Halls, Phys. Rev. Lett. 90 (19) (2003).
[228] A. Mahreni et al., J. Membr. Sci. 327 (1–2) (2009) 32–40.
[229] C. Zhao et al., J. Power Sources 194 (1) (2009) 168–174.
[230] K. Schmidt-Rohr, Q. Chen, Parallel cylindrical water nanochannels in Nafion fuel-cell membranes, in: Materials for Sustainable Energy: A Collection of Peer-Reviewed Research and Review Articles, Nature Publishing Group, 2011, pp. 238–246.
[231] S. Yun et al., J. Membr. Sci. 380 (1–2) (2011) 208–215.
[232] S. Yun et al., J. Appl. Polym. Sci. 126 (S2) (2012) E513–E521.
[233] M.S. Asgari et al., Int. J. Hydrogen Energy 38 (14) (2013) 5894–5902.
[234] H. Zhang et al., Int. J. Hydrogen Energy 39 (2) (2014) 974–986.
[235] L. Cui et al., Polym. Adv. Technol. 26 (5) (2015) 457–464.
[236] M.M. Hasani-Sadrabadi et al., Nano Energy 23 (2016) 114–121.
[237] M. Amjadi et al., Int. J. Hydrogen Energy 35 (17) (2010) 9252–9260.
[238] Q. Li et al., J. Membr. Sci. 423 (2012) 284–292.
[239] A. Aslan, A. Bozkurt, Solid State Ionics 255 (2014) 89–95.
[240] D. Cozzi et al., J. Power Sources 248 (2014) 1127–1132.
[241] H. Wu et al., J. Power Sources 273 (2015) 544–553.
[242] A. Sacca et al., J. Power Sources 152 (2005) 16–21.
[243] K. Hooshyari et al., J. Power Sources 276 (2015) 62–72.
[244] J. Auimviriyavat, S. Changkhamchom, A. Sirivat, Ind. Eng. Chem. Res. 50 (22) (2011) 12527–12533.
[245] Y. Devrim, A. Albostan, Int. J. Hydrogen Energy 40 (44) (2015) 15328–15335.
[246] A. Chandan et al., J. Power Sources 231 (2013) 264–278.
[247] R.E. Rosli et al., Int. J. Hydrogen Energy 42 (14) (2017) 9293–9314.
[248] Y. Wang, C.Y. Wang, Electrochim. Acta 51 (19) (2006) 3924–3933.
[249] T.A. Trabold et al., Int. J. Heat Mass Transfer 49 (25–26) (2006) 4712–4720.
[250] J.P. Owejan et al., Int. J. Heat Mass Transfer 49 (25–26) (2006) 4721–4731.
[251] P. Krüger et al., J. Power Sources 196 (12) (2011) 5250–5255.
[252] T. Sasabe et al., Electrochem. Commun. 13 (6) (2011) 638–641.
[253] J. Mishler et al., Electrochim. Acta 65 (2012) 127–133.
[254] M.A. Hickner et al., J. Electrochem. Soc. 153 (5) (2006) A902–A908.
[255] M.A. Hickner et al., J. Electrochem. Soc. 155 (3) (2008) B294–B302.
[256] M.A. Hickner et al., J. Electrochem. Soc. 155 (4) (2008) B427–B434.
[257] M.A. Hickner, K.S. Chen, N.P. Siegel, J. Fuel Cell Sci. Technol., 7 (2010) 011001-1–011001-5.
[258] M.A. Hickner et al. 157(1) (2010) B32–B38.
[259] E.H. Lehmann, P. Boillat, A. Kaestner, P. Vontobel, D. Mannes, Neutron imaging methods for the investigation of energy related materials-Fuel cells, battery, hydrogen storage and nuclear fuel, in: EPJ Web of Conferences (vol. 104), EDP Sciences, 2015, p. 01007.
[260] Y. Wang, C.Y. Wang, J. Electrochem. Soc. 153 (6) (2006) A1193–A1200.
[261] Y. Wang, K.S. Chen, J. Power Sources 315 (2016) 224–235.
[262] J.T. Gostick et al., Electrochem. Commun. 11 (3) (2009) 576–579.
[263] J. Lee et al., J. Electrochem. Soc. 162 (7) (2015) F669–F676.
[264] C. Hartnig et al., Appl. Phys. Lett. 92 (13) (2008).
[265] Y. Wang, K.S. Chen, J. Electrochem. Soc. 158 (11) (2011) B1292–B1299.
[266] P. Oberholzer et al., Electrochem. Commun. 20 (2012) 67–70.
[267] J. Cho et al., Appl. Energy 111 (2013) 300–309.
[268] A. Öztürk et al., Int. J. Hydrogen Energy 42 (33) (2017) 21226–21249.
[269] Z. Niu et al., Appl. Energy 232 (2018) 443–450.
[270] Y. Wang, C.Y. Wang, J. Electrochem. Soc. 152 (2) (2005) A445–A453.
[271] L. Chen et al., Numer. Heat Transfer, Part A: Appl. 62 (4) (2012) 295–318.
[272] M.S. Hossain, B. Shabani, C.P. Cheung, Int. J. Hydrogen Energy 42 (8) (2017) 5272–5283.
[273] S.G. Kandlikar et al., J. Power Sources 194 (1) (2009) 328–337.
[274] K.S. Chen, M.A. Hickner, D.R. Noble, Int. J. Energy Res. 29 (2005) 11113–11132.
[275] L. Chen, Y.L. He, W.Q. Tao, Int. J. Heat Mass Transfer 60 (2013) 252–262.
[276] S.C. Cho, Y. Wang, K.S. Chen, J. Power Sources 206 (2012) 119–128.
[277] S.C. Cho, Y. Wang, K.S. Chen, J. Power Sources 210 (2012) 191–197.
[278] P. Polverino, A. Esposito, C. Pianese, Int. J. Hydrogen Energy 38 (21) (2013) 8934–8953.
[279] X.C. Adroher, Y. Wang, J. Power Sources 196 (22) (2011) 9544–9551.
[280] S.C. Cho, Y. Wang, Int J. Heat Mass Transfer 71 (2014) 349–360.
[281] S. Malhotra, S. Ghosh, Exp. Therm. Fluid Sci. 100 (2019) 233–250.
[282] M. Andersson et al., Int. J. Hydrogen Energy 43 (5) (2018) 2961–2976.
[283] S. Bhardwaj, A. Dalal, Eur. J. Mech. B. Fluids 72 (2018) 328–339.
[284] A. Jarauta et al., J. Power Sources 323 (2016) 201–212.
[285] S.C. Cho, Y. Wang, Int. J. Heat Mass Transfer 70 (2014) 340–352.
[286] J.M. Lewis, Y. Wang, Int. J. Hydrogen Energy 43 (36) (2018) 17444–17460.
[287] G. Zhang et al., Int. J. Energy Research 42 (15) (2018) 4697–4709.
[288] E. Afshari, M. Mosharaf-Dehkordi, H. Rajabian, Energy 118 (2017) 705–715.
[289] T. Wilberforce et al., Sci. Total Environ. 678 (2019) 728–740.
[290] Y. Wang, C.Y. Wang, Electrochim. Acta 50 (6) (2005) 1307–1315.
[291] I.K.P. Arias et al., Int. J. Hydrogen Energy 42 (24) (2017) 15818–15827.
[292] Y. Wang, C.Y. Wang, J. Electrochem. Soc. 154 (7) (2007) B636–B643.
[293] N. Belgacem, M. Prat, J. Pauchet, Int. J. Hydrogen Energy 42 (12) (2017) 8150–8165.
[294] M. Klages et al., J. Power Sources 239 (2013) 596–603.
[295] R. Banerjee, N. Ge, J. Lee, M.G. George, H. Liu, D. Muirhead, et al., *ECS Trans* 75 (14) (2016) 251–259.
[296] J. Mishler et al., J. Electrochem. Soc. 160 (6) (2013) F514–F521.
[297] Y. Wang, Electrochim. Acta 75 (2012) 239–246.
[298] Y. Wang, S.C. Cho, J. Electrochem. Soc. 160 (10) (2013) A1847–A1855.
[299] Y. Wang, H. Yuan, J. Electrochem. Soc. 164 (9) (2017) A2283–A2289.
[300] Z. Wan et al., Energies 7 (5) (2014) 3179–3203.
[301] A.A. Amamou et al., IEEE Access 4 (2016) 4989–5002.
[302] Y. Luo, K. Jiao, Prog. Energy Combust. Sci. 64 (2018) 29–61.
[303] N. Macauley et al., J. Electrochem. Soc. 163 (13) (2016) F1317–F1329.
[304] R. Borup et al., Chem. Rev. 107 (10) (2007) 3904–3951.
[305] J.P. Sabawa, A.S. Bandarenka, Electrochim. Acta 311 (2019) 21–29.
[306] M.F. Mathias, J. Roth, J. Fleming, W. Lehnert, Diffusion Media Materials and Characterization. Handbook of Fuel Cells—Fundamentals, Technology and Applications, 3, 517–537.
[307] X. Luo et al., Appl. Energy 137 (2015) 511–536.
[308] T. Jahnke et al., J. Power Sources 304 (2016) 207–233.

[309] Y. Wang, J. Power Sources 185 (1) (2008) 261–271.
[310] C.H. Park et al., Nature 532 (7600) (2016) 480.
[311] L. Hao, P. Cheng, Int. J. Heat Mass Transfer 55 (1–3) (2012) 133–139.
[312] C. Si et al., J. Chem. (2015).
[313] R. Flückiger et al., Electrochim. Acta 56 (5) (2011) 2254–2262.
[314] Z. Niu et al., J. Electrochem. Soc. 165 (9) (2018) F613–F620.
[315] J.E. Steinbrenner et al., J. Power Sources 196 (11) (2011) 5012–5020.
[316] A. Bozorgnezhad et al., Int. J. Hydrogen Energy 41 (42) (2016) 19164–19181.
[317] Y. Wang et al., Electrochim. Acta 55 (8) (2010) 2636–2644.
[318] Y. Tabe et al., J. Electrochem. Soc. 163 (10) (2016) F1139–F1145.
[319] I. Mayrhuber et al., ChemElectroChem 2 (10) (2015) 1551–1559.
[320] Kia Motros Corp, Fuel Cell Electric Vehicle, Changing the Hystory <http://m.kia.com/worldwide/about_kia/eco_dynamics/hydrogen_fuel_cell_cars.do>, Internet Publication, 2015.
[321] M. Doran, Engineering the Extreme Capability of the Colorado ZH2, Internet Publication, 2016. <https://media.chevrolet.com/media/us/en/chevrolet/news.detail.html/content/Pages/news/us/en/2016/oct/1101-zh2.html>.
[322] T. Swan, 2017 Chevrolet Colorado ZH2: GM's Military Role Fuel Cell Bows, Internet Publication, 2016. <https://www.kbb.com/car-news/all-the-latest/2017-chevrolet-colorado-zh2-gm-military-role-fuel-cell-bows/2100001203/>.
[323] U.S. Department of Energy, Compare fuel cell vehicles, Internet Publication, 2018. <https://www.fueleconomy.gov/feg/fcv_sbs.shtml>.
[324] Air Force Technology, Stalker XE Unmanned Aerial System (UAS), Internet Publication, 2015. <https://www.airforce-technology.com/projects/stalker-xe-unmanned-aerial-system-uas/>.
[325] H.A. Gasteiger et al., Appl. Catal., B 56 (1–2) (2005) 9–35.
[326] F. Gao, B. Blunier, A. Miraoui, Proton Exchange Membrane Fuel Cells Modeling, John Wiley & Sons, 2013.
[327] A. El-Kharouf, N.V. Rees, R. Steinberger-Wilckens, Fuel Cells 14 (5) (2014) 735–741.
[328] J. Norley, Graphite – Based Bipolar Plates for PEM Motive Fuel Cell Applications, US Department of Energy Bipolar Plates Workshop, 2017.
[329] J.P. Kopasz, T.G. Benjamin, D. Schenck, 2017 Bipolar Plate Workshop Summary Report (No. ANL-17/12), Argonne National Lab. (ANL), Argonne, IL (United States), 2017.
[330] U.S. Department of Energy, DOE Technical Targets for Polymer Electrolyte Membrane Fuel Cell Components, Internet Publication, 2016. <https://www.energy.gov/eere/fuelcells/doe-technical-targets-polymer-electrolyte-membrane-fuel-cell-components>.
[331] H.S. Das, C.W. Tan, A.H.M. Yatim, Renewable Sustainable Energy Rev. 76 (2017) 268–291.
[332] B. Lakshmanan, Balance of Plant (BoP) Components Validation for Fuel Cells, The U.S. Department of Energy Hydrogen Component and System Qualification Workshop Held, 2010.
[333] R.C. Chu et al., IEEE Trans. Device Mater. Reliab. 4 (4) (2004) 568–585.
[334] Y. Wang, C.Y. Wang, J. Power Sources 153 (1) (2006) 130–135.
[335] G. Zhang, S.G. Kandlikar, J. Hydrogen Energy 37 (3) (2012) 2412–2429.
[336] I.P. Jain, C. Lal, A. Jain, Int. J. Hydrogen Energy 35 (10) (2010) 5133–5144.
[337] B. Abderezzak, Introduction to Transfer Phenomena in PEM Fuel Cells, Elsevier, 2018.
[338] K. Jiao, X. Li, Prog. Energy Combust. Sci. 37 (3) (2011) 221–291.
[339] G. Zhang, K. Jiao, J. Power Sources 391 (2018) 120–133.